DOI: https://doi.org/10.2138/am-2023-9271. http://www.minsocam.org/

Revision 2

Transcrustal magmatic system in lamprophyre dyke constructed by multiple magma reservoirs

Xiangsong Wang[1], Yannan Wang[1*], Min Sun[1], Guochun Zhao[1], Keda Cai[3], Xijun Liu[4,5], Zhenglin Li[4], Yunying Zhang[6], Fenn Leppard[1]

[1]NWU-HKU Joint Centre of Earth and Planetary Sciences, Department of Earth Sciences, University of Hong Kong, Hong Kong SAR, China

[2]Key Laboratory for Resource Exploration Research of Hebei Province, Hebei University of Engineering, Handan 056038, China

[3]State Key Laboratory of Geological Processes and Mineral Resources, and School of Earth Science and Resources, China University of Geosciences, Beijing 100083, China

[4]Guangxi Key Laboratory of Hidden Metallic Ore Deposits Exploration, Guilin University of Technology, Guilin 541004, China

[5]Xinjiang Research Center for Mineral Resources, Xinjiang Institute of Ecology and Geography, Chinese Academy of Sciences, Urumqi 830011, China

[6]South China Sea Institute of Oceanology, Chinese Academy of Sciences, Guangzhou 510301, China

ABSTRACT

The mineral assemblages, chemistry and textures of igneous rocks can record crucial information on magmatic processes in transcrustal magmatic systems. To effectively identify such processes, we present systematic petrological, mineralogical, and geochronological data for a suite of lamprophyre dykes that intruded early flood basalts in the Tuoyun basin of Western Tianshan. The lamprophyre dykes show ocean island basalt-like trace element patterns and depleted Sr–Nd isotope compositions, suggesting that they were derived from a depleted mantle source. Apatite U-Pb dating reveals that the lamprophyre dykes were emplaced at 66 Ma. These lamprophyre dykes consist of three groups of mineral assemblages: (I) Type-I Clinopyroxene (Cpx); (II) Amphibole (Amp) core and Apatite (Ap); and (III) Amp rim, Type-II Cpx, K-feldspar (Kfs) and Plagioclase (Pl). These mineral assemblages are in chemical disequilibrium and correspond to three magma reservoirs within the transcrustal magmatic system. Textural and geochemical features demonstrate that Type-I Cpx represents antecrysts captured from lower crustal crystal mushes. The Amp cores have the same rare earth element patterns as their enclosed Type-I Cpx inclusions, demonstrating that the Amp cores were produced through peritectic reactions consuming Cpx. The third assemblages occur as microlites that formed by the shallow crystallization of evolved melts. Thermobarometric calculations suggest a lower crust magma reservoir at 20–30 km depth, a middle crust magma reservoir at ~15 km depth, and a shallow upper crust magma reservoir at <5 km depth, making up a magma plumbing system of the lamprophyre dykes. The transcrustal magmatic system

involves multiple stages of open-system processes, including the recycling of early-formed crystals, multiple magma replenishment, peritectic reactions, and crystal fractionation, resulting in the formation of lamprophyre dykes.

Keywords: lamprophyre dykes; transcrustal magmatic system; antecrysts; peritectic reactions, Western Tianshan

INTRODUCTION

Magmatic systems form in various tectonic settings by magma fluxing into and through the crust, giving rise to the formation of intrusive rocks and volcanic activities. Geophysical, geochemical, and petrological studies demonstrate that the magma reservoirs dominantly consist of crustal mush that may be stored at near-solidus temperature conditions (e.g., Cashman and Blundy, 2013; Cooper and Kent, 2014; Costa et al., 2009; White and McCausland, 2016). A novel conceptual model, known as the transcrustal magmatic systems, has been proposed recently (Cashman et al., 2017; Edmonds et al., 2019; Sparks et al., 2019). This model emphasizes the presence of multiple magma reservoirs that develop throughout the crust within a volumetrically dominant crystal mush system. In the transcrustal magmatic system, the high ambient temperature and low-viscosity melts in the lower crust promote pronounced compaction-driven melt segregation and reactive flow. Consequently, destabilization of melt lenses is anticipated in the middle crust, leading to episodic and rapid magma recharge to upper crustal magma reservoirs (Cashman et al., 2017).

Mafic and intermediate to silicic magmatic systems exhibit distinct differences in terms of their chemical compositions, physical properties, and eruptive behavior (e.g., Cashman and Giordano, 2014). Previous studies suggest that intermediate to silicic magma systems often involve multiple magma reservoirs, while mafic magmas may either erupt directly from source to surface or involve fewer magma reservoirs, due to the faster ascent of mafic magmas compared to felsic magmas, as well as their lower viscosity, greater fluidity, and ability to exploit existing fractures in the crust (e.g., Bachmann and Huber, 2016; Bryan et al., 2010). However, recent studies suggest that mafic magmas can indeed form multiple magma reservoirs (e.g., Ubide et al., 2014a, 2014b, 2019; Xing and Wang, 2020). The development of these reservoirs is influenced by factors such as the local stress regime, the presence of pre-existing structures, and the rate of magma supply (e.g., Anderson et al., 2019).

Understanding the processes of magma generation, transportation, storage, crystallization, and reactivity within the transcrustal magmatic system is crucial for comprehending the sources and evolution of magmas, which govern their geochemical and lithological variability (e.g., Xing and Wang, 2020). However, identifying the dominant magmatic processes controlling the evolution of mafic magmas is relatively intricate, as the geochemical characteristics of the magma sources and deep magma reservoirs are commonly overprinted by late-stage magma differentiation and mixing processes. Fortunately, the crystal cargo, including cumulate nodules, glomerocrysts, and antecrysts, provides invaluable insights into magma accumulation, crystal mush rejuvenation and magma differentiation, offering new perspectives on the evolution of magma plumbing systems (e.g., Xing and Wang, 2020, Wang et al., 2019).

The lamprophyres are present in minor volumes but widely distributed in orogenic belts and within-plate settings (e.g., Ubide et al., 2012). They carry crucial information about the nature of the mantle and mantle processes, with their primitive compositions potentially representing parental magmas from the mantle source (e.g., Dai et al., 2021; Owen, 2007). However, recent studies highlight the need for caution when making such assumptions, as whole-rock analysis provides mean compositions of multiple geochemically distinct components, obscuring the complexity and variation of the magma system (e.g., Reubi and Blundy, 2009; Ubide et al., 2012; Ubide et al., 2014a). Lamprophyre dykes commonly host multiple crystal populations, which gather and mix with host melts in a transcrustal magmatic system. The abundant phenocrysts and antecrysts in these dykes generally record the physical and chemical characteristics of magma reservoirs, providing a window to study magmatic processes within the magma plumbing systems.

In this paper, we present a detailed petrological, mineralogical, and geochronological study of lamprophyre dykes that crop out in the Tuoyun basin, southwestern Tianshan. These data illustrate a comprehensive picture of the spatial-temporal evolution of a transcrustal magmatic system extending through the crust for the lamprophyre dyke.

GEOLOGICAL BACKGROUND AND PETROGRAPHY

DOI: https://doi.org/10.2138/am-2023-9271. http://www.minsocam.org/

The Western Tianshan orogenic belt (WTOB) is located in northwestern China, Kyrgyzstan, Uzbekistan, Tajikistan and the southern part of Kazakhstan. It records long-term multi-stage tectonic evolution, such as the accretion and collision in the Paleozoic, intracontinental modification in the Mesozoic, and crustal deformation and rapid uplift in the Cenozoic (e.g., Windley et al., 2007; Xiao et al., 2015). It can be tectonically divided into three subunits from north to south: the North Tianshan Belt, the Middle Tianshan Belt, and the South Tianshan Belt (Fig. 1a). The North Tianshan Belt includes Precambrian continental fragments and Early Paleozoic ophiolites extensively intruded by Paleozoic granitoids (Kröner et al., 2013). The Middle Tianshan Belt is characterized by Precambrian basement with Paleozoic intrusive rocks (Gao et al., 1998). The South Tianshan Belt is considered as a late Paleozoic accretionary complex (Han et al., 2015).

Despite being relatively small in volume, the intraplate basalt province in the Western Tianshan covers an area exceeding 285,000 km^2 and formed during the Late Cretaceous and Cenozoic periods (Simonov et al., 2008). The basaltic rocks commonly occur as dykes and stocks intruding Paleozoic-Mesozoic rocks, or as flows and sills within the Cretaceous-Paleocene sedimentary sequences (Simonov et al., 2015; Sobel and Arnaud, 2000). The Tuoyun intermontane basin is tectonically located in the South Tianshan Belt, north of the North Tarim fault and east of Talas-Ferghana Strike-slip fault (Fig. 1a). The Jurassic, Cretaceous and Tertiary strata are distributed in the basin, which are in angular unconformable contact with Late Silurian-Early Carboniferous strata. The Tuoyun basin is a compound volcanic basin that consist of the basaltic intrusive rocks, which are emplaced in Jurassic-Lower Cretaceous sedimentary rocks, and basaltic extrusive rocks (flood basalts) that unconformably overlain the Paleogene sedimentary rocks (Fig. 1b) (Liang et al., 2004). These basaltic rocks belong to the alkali series and mainly include picrobasalt, basalt, basanite, tephrite, and phonolite (Ji et al., 2006). In the field, two separate series of basalt flows have been distinguished (Fig. 1b). Previous studies have suggested that the lower basalt series was formed at 120–110 Ma, while the upper basalt series was constrained to 67–46 Ma, based on whole-rock and mineral $^{40}Ar/^{39}Ar$ and K-Ar dating (e.g., Sobel and Arnaud, 2000).

In this study, newly identified lamprophyre dykes were found to intrude the lower basalt series. The basalts are dark gray and show a massive structure, with phenocrysts of olivine and clinopyroxene. The lamprophyre dykes vary in thicknesses from 0.5 to 1 m (Fig. 2a), and are characterized by fresh, porphyritic texture (Fig. 2b). The primary phenocryst within the lamprophyres is amphibole (Amp: 40–50 vol%), which is randomly distributed within an aphanitic or fine-grained aphanitic matrix. The phenocrystic Amp is euhedral and mostly elongated in thin sections, about 0.5–3 mm in length and 0.2–0.5 mm in width (Fig. 2c and 2d). Significantly, the majority of the phenocrystic Amp grains show strong disequilibrium textures, such as normal zoning, and contain irregularly shaped Cpx inclusions (50 to 500 μm) with embayed edges and resorption channels. In contrast, some phenocrystic Amp grains appear homogeneous and lack visible zoning (see the back-scattered electron (BSE) images below).

Microcrysts of K-feldspar (Kfs: ~30–40 vol%), plagioclase (Pl: ~30–40 vol%), clinopyroxene (Cpx: ~10–15 vol%), apatite (Ap: ~5 vol%) and minor Fe-Ti oxides make up 80–90 vol% of the matrix. The K-feldspar and plagioclase microcrysts are commonly 0.1–1 mm in length, and the Fe-Ti oxides microcrysts have grain sizes ranging from 10 to 100 μm. The Cpx microcrysts are typically anhedral, and occur as discrete grains in the matrix with sizes < 0.1 mm. The euhedral and acicular Ap grains are widely distributed as inclusions within phenocrystic Amp or as microlites within the matrix, and range in length from 0.1 to 2 mm (Fig. 2c and 2d).

ANALYTICAL METHODS

An integrated study was conducted on the lamprophyres from the Tuoyun basin, encompassing apatite U-Pb ages, whole-rock major and trace elements, Sr-Nd isotope compositions, and mineral major and trace elements.

Apatite U-Pb analyses were performed at the Beijing Quick-Thermo Science & Technology Co., Ltd, using an ESI New Wave NWR 193^{UC} (TwoVol2) laser ablation system connected to an Agilent 8900 ICP–QQQ following analytical procedures described in Ji et al. (2020). Individual apatite grains (mounted and polished in epoxy) were ablated in a constant stream of He that is mixed downstream with N_2 and Ar before entering the torch region of the ICP–QQQ. After warmup of the ICP–QQQ and connection with the laser ablation system, the ICPMS is first tuned for robust plasma conditions by optimizing laser and ICP–QQQ setting, monitoring $^{232}Th^{16}O^+/^{232}Th^+$ ratios (always ≤0.2%) and $^{238}U^+/^{232}Th^+$ ratios (always between 0.95 and 1.05) while ablating NIST SRM 612 in line scan mode.

During U-Pb age determination, apatite Madagascar were used as primary reference materials, apatite McClure Mountain were used as secondary reference materials. NIST610 and NIST612 glasses were used to calibrate trace element with internal standard major element Ti, Si or Ca. The spot size and frequency of the laser were set to 45 μm and 5 Hz, respectively. The reference materials were analyzed two times before and after each analytical session including 6-8 spots on minerals. Background subtraction and correction for laser downhole elemental fractionation were performed using the Iolite data reduction package within the Wavemetrics Igor Pro data analysis software (Paton et al., 2010). Concordia diagrams (Wetherill and Tera-Wasserburg) were processed using ISOPLOT 4.15. The results are presented in Table S1.

Major and trace elements were analyzed at the ALS Chemex Company in Guangzhou. Major elements were obtained by X-ray fluorescence spectrometry (XRF) using fused lithium tetraborate glass pellets. Loss on ignition (Loiselet et al., 2009) values was measured using 1 g of powder heated to 1100°C for 1 h. The accuracy of the analyses is within 1% for most major elements, which is determined on the Chinese National standard GSR-3. Trace elements, including rare earth elements (REE), were analyzed by inductively coupled plasma-mass spectrometry (ICP-MS). About 50 mg of powdered sample was placed in a steel-bomb with mixed HF + HNO3 acid for 48 h in order to assure complete dissolution of the refractory minerals under high pressure. Analytical precision was generally better than 5 %. The major and trace element data are presented in Table S2.

Whole-rock Sr-Nd isotope analyses were performed on a Neptune Plus MC-ICP-MS (Thermo Fisher Scientific, Dreieich, Germany) at the Wuhan Sample Solution Analytical Technology Co., Ltd, Hubei, China. The exponential law, which initially was developed for TIMS measurement (Russell et al. 1978) and remains the most widely accepted and utilized with MC-ICP-MS, was used to assess the instrumental mass discrimination in this study. The international NIST 987 and GSB 04-3258-2015 standards were measured every seven samples analyzed for Sr and Nd isotope, respectively. All data reduction for the MC-ICP-MS analysis of Sr-Nd isotope ratios was conducted using "Iso-Compass" software (Zhang et al. 2020). Analyses of the NIST 987 standard solution yielded $^{87}Sr/^{86}Sr$ ratio of 0.710242±14 (2SD, n=345), which is identical within error to their published values 0.710248±12 (Zhang and Hu, 2020). Analyses of the GSB 04-3258-2015 standard yielded $^{143}Nd/^{144}Nd$ ratio of 0.512440±6 (2SD, n=31), which is identical within error to their published values (0.512438±6 (2SD) Li et al., 2017). The results are presented in Table S3.

Mineral compositions were conducted at the Department of Earth Sciences, the University of Hong Kong, using a JEOL JXA-8230 electron microprobe. An accelerating voltage of 15 kV, a specimen current of 3.0×10^{-8} A and a beam size of 1 μm were employed. The analytical errors are generally less than 2%. All data were corrected using standard ZAF correction procedures and the detailed analytical procedures are similar to those described by Li and Zhou (2018). The mineral compositions are presented in Tables S4, S6, S8 and S10.

In situ mineral trace-element compositions were determined using an ELEMENT XR (Thermo Fisher Scientific) ICP–MS coupled with a 193-nm (ArF) Resonetics RESOlution M-50 laser ablation system at the Guangxi Key Laboratory of Hidden Metallic Ore Deposits Exploration, Guilin University of Technology. Laser condition was set as following: beam size, 45μm; repetition rate, 6 Hz; energy density, ~4 J cm^{-2}. A smoothing device (The Squid, Laurin Technic) was used to smooth the sample signal. Each spot analysis consisted of 20 s gas blank collection with the laser off, and 30 s sample signal detection with the laser on. More details on the experiment procedure and data reduction strategy are described in detail by Zhang et al. (2019). Trace element concentrations were calibrated using multiple reference materials (BCR-2G, BHVO-2G, and GSD-1G) as external standards, and Si as the internal standard element. Off-line selection and integration of background and analyte signals, time-drift corrections and quantitative calibrations were undertaken using ICPMSDataCal (Liu et al., 2010). The results are given in Tables S5, S7 and S9.

Fractional crystallization process (includes equilibrium and disequilibrium fractionation in hydrous and anhydrous systems) was modeled by phase equilibrium simulator (GeoPS) (Xiang and Connolly, 2022) in the Na_2O-CaO-K_2O-FeO-MgO-Al_2O_3-SiO_2-H_2O-TiO_2-O_2 (NCKFMASHTO) chemical system, using the thermodynamic database from Holland and Powell (2011) (hp622ver.dat). Activity-composition solution models were as follows: melt [melt (HGP)], amphibole [cAmph (G)], clinopyroxene [Cpx (HGP)], garnet [Gt (HGP)], ilmenite [Ilm (W)], feldspar [Fsp (Cl)], epidote [Ep (HP11)]. We assume sample C19TY28, which has the most

DOI: https://doi.org/10.2138/am-2023-9271. http://www.minsocam.org/

primitive, highest MgO compositions, as starting compositions, and assess whether its liquid line of descent passes through the more evolved compositions.

RESULTS

Apatite U-Pb ages

Apatite grains from the lamprophyres are euhedral, gray in color, and occur as prismatic crystals with lengths ranging from 50 to 300 μm and widths between 30 and 50 μm. The backscattered electron (BSE) images show all the apatite grains are homogenous and bright without oscillatory zoning and mineral inclusions. They have uniform U (5–12 ppm) and Th (12–23 ppm) contents with Th/U ratios of 1.8–2.7 (Table S1). The apatite U-Pb dating results in linear arrays on the Tera-Wasserburg Concordia plots, yielding a lower intercept age of 66.2 ± 6.3 Ma (MSWD = 0.55) (Fig. 3). This age is considered representative of the emplacement timing for the Tuoyun lamprophyres.

Whole-rock major and trace elements

The Tuoyun lamprophyres have uniform major-oxide compositions with low silica (SiO_2 = 45.5–46.7 wt%) and high alkali (Na_2O+K_2O = 8.1–8.9 wt%) contents (Table S2). In the TAS diagram, they mainly plot within the tephrite field, classifying them as alkaline lamprophyres (Fig. 4). These rocks have high contents of TiO_2 (1.8–2.4 wt%), $Fe_2O_3^T$ (10.0–11.9 wt%) and Na_2O (4.7–5.1 wt%), but low MgO (3.4–4.1 wt%). Their chondrite-normalized rare earth element (REE) patterns are characterized by pronounced enrichments of light REEs ($(La/Yb)_N$ = 13.8−16.0), with slightly positive Eu anomalies (Eu/Eu* = $2Eu_N/(Sm_N+Gd_N)$ = 1.0 − 1.1). They exhibit significant peaks at Nb and Ta, and troughs at Ti and Pb in the primitive mantle-normalized spidergrams, resembling those of ocean island basalts (OIBs) (Fig. 5a and 5b) (Sun and McDonough, 1989).

Whole-rock Sr–Nd isotope compositions

The Tuoyun lamprophyres show low and uniform initial $^{87}Sr/^{86}Sr$ ratios (0.7043–0.7044), and yield relatively uniform Nd isotopic compositions with high $\varepsilon_{Nd}(t)$ values (+5.0 to +5.3) (Table S3; Fig. S1). The Sr–Nd isotope compositions of the Tuoyun lamprophyres are similar to those of the Tuoyun basalts (Fig. S1).

Mineral compositions

Clinopyroxene

Two types of clinopyroxene (Cpx) have been identified for the lamprophyres (Fig. 6). Type-I Cpx is texturally present as inclusions within large Amphibole (Amp) phenocrysts or large crystals with Amp reaction rim, while Type-II Cpx occurs as microlites and small crystals (<100 μm) within the matrix of the lamprophyres (Fig. 6). Type-I Cpx has a diopsidic composition (Fig. 7a) with relatively high Mg# ($Mg/[Mg+Fe^{2+}]$) values (68−75), TiO_2 (1.1−5.5 wt%) and Al_2O_3 (3.4−9.6 wt%) contents, but low FeO (7.9−10.1 wt%) contents (Table S4). Type-I Cpx has bell-shaped chondrite-normalized REE patterns that are LREE and HREE-depleted relative to MREE with slightly positive to negative Eu anomalies (Eu/Eu* = 0.8–1.1) (Table S5; Fig. 5c). Type-I Cpx is characterized by positive Zr, Hf, and Ti anomalies, and negative Sr anomalies in the primitive mantle-normalized patterns (Fig. 5d).

Type-II Cpx plots into hedenbergite-augite field (Fig. 7a) with lower Mg# (19–34) values, TiO_2 (0.1–0.4 wt%) and Al_2O_3 (0.5–1.4 wt%) contents, and higher FeO (19.7–23.4 wt%) contents than Type-I Cpx (Table S4). Its chondrite-normalized REE patterns are characterized by convex-upward LREE pattern with $(La/Sm)_N$ ratios ranging from 5.59 to 8.95 and marked negative Eu anomalies (Eu/Eu* = 0.5–0.8). The primitive mantle-normalized trace-element patterns show that they are enriched in Zr, Hf, Th and U and depleted in Nb, Ta, Sr and Ti elements (Fig. 5c and 5d).

The Cpx grains in flood basalt plot into clinoenstatite field (Fig. 7a). They are characterized by variable and higher Mg# (73–91), CaO (18.7–22.9 wt%), and lower FeO (2.8–8.0 wt%) contents than Type-I Cpx.

Amphibole

Amp occurs as a reaction rim with Cpx and phenocrysts in the lamprophyres (Fig. 6). Two distinct types of Amp can be distinguished based on their internal structures, i.e. Type-I exhibits a core-rim structure and Type-II lacks a zoning structure. They are all calcic with $Ca_B > 1.5$; $(Na+K)_A > 0.5$; Ti = 0.27 to 0.78 atoms per formula unit (apfu) calculated by Ridolfi et al. (2018), and can be classified as kaersutite-feeropargasite (Table S6; Fig. 7b) according to the nomenclature of Leake et al. (1997). The core of type-I Amp exhibit higher Mg# (54.1–66.7), MgO (10.0–12.4

wt.%), Al_2O_3 (11.8–12.5 wt.%) and TiO_2 (4.4–6.8 wt.%), but lower FeO^T (10.9–15.5 wt.%) contents than the rim of type-I Amp (Fig. 8). The core of type-I Amp has bell-shaped chondrite-normalized REE patterns that are slightly LREE- and HREE-depleted relative to MREE (Fig. 5e) with slightly positive to negative Eu anomalies (Eu/Eu* = 0.9–1.2). The primitive-mantle-normalized trace-element patterns show that they are enriched in Ba, Sr, Nb, Ta, and Ti elements, and depleted in Th and U elements (Table S7; Fig. 5f). The rim of type-I Amp shows lower Mg# (19.8–55.3), MgO (3.7–10.0 wt.%), and TiO_2 (2.3–5.2 wt.%), but higher FeO^T (14.2–26.1 wt.%) contents (Fig. 8). Their chondrite-normalized REE patterns exhibit enrichment in LREEs ($(La/Yb)_N$=4.9–19.7) with negative Eu anomalies (mostly Eu/Eu* = 0.8–1.0) (Fig. 5e). The primitive-mantle-normalized trace-element patterns demonstrate depletion of Sr, and enrichment of Nb, Ta and Ti (Fig. 5f).

Apatite

The euhedral and acicular Apatite (Ap) grains are shown as inclusions in phenocrystic Amp and as microlites in the matrix (Fig. 6g). They have uniform CaO (54.9–55.6 wt.%) and P_2O_5 (42.4–43.5 wt.%), along with high F (0.7–1.2 wt.%) and low Cl (0.2–0.3 wt.%) contents (Table S8), and can be classified as fluorapatite. The apatite grains have LREE-enriched and HREE-depleted patterns with slightly positive to negative Eu anomalies (Eu/Eu* = 0.8–1.1) (Table S9; Fig. S2).

K-feldspar and Plagioclase

Patchy zoning and sieve texture are observed in the core of the Kfs microlite. In backscattered electron (BSE) images, the patchy zoning displays irregular dark and bright domains (Fig. 6h and 6i). The patchy zoned cores of the Kfs have abundant spongy spaces that are filled with Ap and matrix materials (Fig. 6i). The Kfs microlites have core-rim structure with orthoclase (Or = K/(Ca+Na+K) = 95 – 99) in the core, and sanidine (Or = 47 – 58) in the rim (Table S10; Figs. 6i and 7c). In contrast, the Pl is almost albite (Ab) in composition, with Ab content (Ab = Na/(Ca+Na+K)) ranging from 94 to 99 (Table S10; Fig. 7c).

DISCUSSION

Timing and origin of the intraplate lamprophyre dykes in the Western Tianshan

The Western Tianshan orogenic belt (WTOB) is predominantly composed of arc magmatic rocks formed by the subduction of Paleo-Tianshan oceanic crust during the Paleozoic. These rocks are characterized by significant enrichment in large ion lithophile elements (e.g. Rb, Sr and Ba) and depletion in high field strength elements (e.g. Nb, Ta and Ti) (e.g., Han and Zhao, 2018; Wang et al., 2020). However, some volumetrically minor mafic rocks with positive Nb and Ta anomalies occur in the WTOB, contrasting with those of the arc magmatic rocks and can be attributed to intraplate genesis. Previous geochronological studies, such as bulk rock K-Ar, bulk rock and biotite $^{40}Ar/^{39}Ar$, and zircon U-Pb dating, yielded ages of 120–110 Ma and 67–46 Ma (Liang et al., 2007; Simonov et al., 2015; Sobel and Arnaud, 2000). The lamprophyres are classified as Si-unsaturated alkaline rocks with low SiO_2 and Zr concentrations, and are commonly zircon-free in the samples. However, the alkaline rocks are generally saturated with apatite (e.g., Ladenburger et al., 2016), making apatites suitable for U-Pb dating. The Ap U-Pb dating yielded an age of 66 ± 6 Ma in this study (Fig. 3), representing the emplacement age of the lamprophyre dykes. The field contact relationship shows that lamprophyre dykes intruded the early flood basalts, suggesting at least two episodic magmatic events occurred in the studied area, which is consistent with the geochronological results.

The Tuoyun lamprophyres have depleted Sr–Nd isotope compositions ($\varepsilon_{Nd}(t)$ = +5.0 to +5.3) resembling those of basalts (Fig. S1), implying that they were derived from a comparable depleted mantle source. However, the presence of abundant Amp phenocrysts in the lamprophyres likely indicates that they originated from a hydrous and depleted mantle source in an intraplate setting.

Sequence of mineral formation in the magmatic reservoir

The Type-I Cpx appears to be in textural disequilibrium with their host rocks, as demonstrated by the presence of resorbed Cpx with embayed edges and overgrowth Type-I Amp rims (Fig. 6), indicating reaction with the host magma. The Type-I Cpx exhibits lower Mg# and CaO contents, and higher TiO_2 and FeO contents than those Cpx of flood basalts, suggesting that Type-I Cpx is not xenocryst from the country rocks. In addition, the Type-I Cpx is characterized by depletion of LREEs and positive Ti anomaly, which is distinct from those of host rocks with enrichment of LREEs and negative Ti anomaly (Fig. 5). The above characteristics indicate that the Type-I Cpx can be described as antecrysts, which did not crystallize from the magma they are now hosted in but were likely recycled from earlier stages of the magmatic system at depth (Davidson et al., 2007b; Ubide et al., 2014b; Zhang et al., 2015). The Type-I Cpx shows gradually increased TiO_2 and Al_2O_3 contents with decreased Mg# values, which are consistent with genesis of cumulates (Fig. 9) (Klaver et al., 2017). Our modeling trends also suggest that the Type-I Cpx grains were unlikely to have formed through magmas equilibrium or disequilibrium fractionation (Fig. 9). In contrast, Type-II Cpx occurs as microcrysts within the matrix and define an opposite evolutionary trend to Type-I Cpx antecrysts, e.g., Type-II Cpx has lower Mg#, TiO_2 and Al_2O_3 values, but higher FeO and REE contents than those of Type-I Cpx (Fig. 9), suggesting they crystallized in the magmas distinctive from those Type-I Cpx crystallized, i.e. Type-I Cpx crystallized in a more primitive magma while Type-II Cpx formed in a more evolved magma. Previous studies have suggested that high-Mg# Cpx occurs as a near-liquidus mineral first within primitive magmas, whereas Cpx with lower Mg# crystallizes in mildly evolved, low-Mg# mafic or intermediate magmas (that underwent prior differentiation) (Blatter et al., 2013; Sisson et al., 2005).

The mineral compositions can help constrain whether the compositional variations within these two types of Cpx were the results of mineral fractionation. The feldspar crystallization preferentially removes Eu and Sr from melts (Aigner-Torres et al., 2007; Icenhower and London, 1996), whereas amphibole crystallization preferentially incorporates middle rare earth elements (MREEs) and Ti element (Bottazzi et al., 1999; Tiepolo et al., 2007). Type-I Cpx shows increased TiO_2 and

Eu/Eu* with decreased Mg# values, as well as relatively uniform Dy and Dy/Yb ratios (Fig. 9), implying that feldspar and amphibole crystallizations were suppressed before and during the formation of Type-I Cpx. These were further supported by a remarkable increase in Type-I Cpx Al_2O_3 content from ~3 wt.% at Mg# 75 to 10 wt.% with Mg# 68 (Fig. 9b), as feldspar crystallization would significantly decrease Al_2O_3 contents in the residual melts. In addition, plagioclase is present as an intercumulus phase in the matrix of lamprophyres, and it has significantly low An content (0 – 4), further suggesting that plagioclase saturation was delayed and it crystallized as a later phase. In contrast, Type-II Cpx has variable Dy concentrations and low Eu/Eu* values, but relatively uniform Dy/Yb ratios (Fig. 9e and 9f), indicating that the compositional variations within Type-II Cpx resulted from feldspar crystallization.

Type-I Cpx is texturally enclosed by Type-I Amp, which indicates Type-I Cpx crystallized earlier than Type-I Amp. However, the REE profiles of Type-I Amp core closely resembled those of Type-I Cpx inclusions (Fig. 5), and the anhedral Type-I Cpx has sub-rounded edges and enclosed by Amp (Fig. 6). These compositional and textural characteristics manifest that the formation of Type-I Amp core as a consequence of the peritectic reaction between Type-I Cpx and the melt (i.e. Cpx + melt = Amp). This is also supported by the comparable Eu/Eu* ratios observed in Type-I Amp core and Type-I Cpx (Figs. 5, 9 and 10). Our modeling of fractionation trends does not align well with the compositions of Type-I Amp core, further suggesting the peritectic reaction genesis of Type-I Amp core (Fig. 10).

In addition, Type-I Amp cores have high Mg# values (54–67) and Al_2O_3

contents (11.8−12.5 wt.%) (Fig. 10b), as well as significant positive Sr anomalies (Figs. 5f and 10e), which suggest that feldspar crystallization did not take place before the formation of both Type-I Amp core and Type-I Cpx. In contrast, both Type-I Amp rim and Type-II Cpx have lower Mg# and Al_2O_3, Eu/Eu*, and Sr/Sr* values relative to their respective Type-I Amp core and Type-I Cpx (Figs. 9 and 10), suggesting that they have crystallized from already differentiated melts associated with the fractional crystallization of feldspar and amphibole.

Ap grains are present as small inclusions within Amp and Kfs phenocrysts or as microlites within the matrix of the lamprophyres (Fig. 6g). The Ap grains show a positive correlation between Eu/Eu* and Sr/Sr* ratios (Fig. S2). These textural relationships and compositional features indicate that Ap crystallization was accompanied by fractional crystallization of amphibole and feldspar.

Based on the aforementioned textual and compositional features of minerals, three distinct mineral assemblages have been identified within the lamprophyres. The first assemblage consists of Type-I Cpx antecrysts, which formed from a more primitive magma and were subsequently captured by the host magmas within the same magmatic system. The second assemblage consists of Type-I Amp core and Ap. The third assemblage includes Type-I Amp rim, Type-II Cpx, Kfs and Ab, which formed from an evolved magma reservoir. Consequently, the established crystallization sequence of the magmatic mineral phases within the lamprophyres is as follows: Type-I Cpx > Type-I Amp core + Ap > Type-I Amp rim + Type-II Cpx + Kfs + Ab.

Crystallization conditions of the lamprophyres

Determining the storage conditions of magmas is crucial for understanding the magmatic plumbing system and the evolutionary process for the lamprophyres. As mentioned above, the formation of lamprophyres involved complicated magmatic processes, including capture of Cpx antecrysts in the deep magma reservoir, early crystallization of Amp, and delayed saturation of plagioclase. These magmatic processes are consistent with the results of previous experimental studies. For example, experimental studies on the differentiation of hydrous basaltic magmas indicate high-aluminous Cpx crystallizes before Amp at higher pressures (0.4−0.7 GPa), while low-aluminous Cpx crystallizes at upper crustal pressures (~0.2 GPa) (Melekhova et al., 2015; Müntener and Ulmer, 2006; Pichavant and Macdonald, 2007; Sisson and Grove, 1993). In this study, Type-I Cpx has higher Al_2O_3 contents than those of Type-II Cpx, implying the elevated crystallization pressures of Type-I Cpx. On the other hand, the stabilities of Amp and Pl in magmas are mainly controlled by H_2O content and pressure. Recent experiments on hydrous mafic-intermediate magmas at high temperatures (Blatter et al., 2017; Ulmer et al., 2018) have revealed that the maximum thermal stability of Amp is around 1100 °C, and early-crystallized Amp can form through a peritectic reaction process. This peritectic reaction can be achieved through consuming the earlier-formed Cpx under high water (≥ 3 wt.%) and pressure (≥ 0.7 GPa) conditions, supporting the idea that the reaction-replacement of Amp observed in this study may have taken place at high pressure and water-rich conditions. Conversely, the stability of plagioclase is suppressed with high pressure and water content (Melekhova et al., 2015; Nandedkar et al., 2014), and its saturation tends to appear at shallow levels (Arculus and Wills, 1980; Sisson and Grove, 1993).

The compositions of Cpx are sensitive to the temperature and pressure conditions during magma crystallization, providing valuable constraints on the crystallization conditions (Neave et al., 2019; Neave and Putirka, 2017; Putirka, 2008). To assess mineral-melt equilibrium among various Cpx compositions and their hosting melt, equilibrium diagrams have been utilized (Fig. 11a). To eliminate the effect of the antecrysts, we choose the major element composition of the groundmass that is best exemplified by the whole rock composition of the dike's chilled margin, comprising a minimal volume fraction of antecrysts (C19TY28 and C19TY29). Considering that the lamprophyre dykes were formed by multiple magma replenishments, even though the high-Mg Cpx (Type-I Cpx) show Fe-Mg exchange equilibrium with their host rocks (Fig. 11a) (K_D[Fe-Mg]=0.28 ± 0.08; Putirka, 2008), the Type-I Cpx belongs to antecrysts and the clinopyroxene-melt thermobarometer cannot be used to estimate the crystallization temperature and pressure of the Type-I Cpx (Neave and Putirka, 2017; Putirka, 2008). Similarly, the Type-II Cpx is also not in equilibrium with the corresponding whole-rock compositions (Fig. 11a). In this study, we applied a recently proposed clinopyroxene-only thermobarometer by Jorgenson et al. (2022), which employs a machine learning algorithm to generate predictive models that applicable to our samples. The crystallization temperature and pressure conditions of the Type-I Cpx were constrained at ~1050–1150 °C and ~6–10 kbar, respectively, while the Type-II Cpx crystallized at temperatures of ~850–925 °C and pressures of ~1–1.2 kbar. These results are consistent with the observation of mineral assemblages that Type-II Cpx crystallized together with feldspar. In addition, the Type-II Cpx possesses significantly lower Mg# and Eu/Eu* values, demonstrating that the Type-II Cpx formed in a shallow level magma reservoir. Besides, the fractional crystallization experimental studies on andesitic melts also reveal that the low-Al Cpx (compositions equivalent to the Type-II Cpx) can be produced at upper crustal pressures (~2 kbar) (Grove et al., 2003), consistent with the case in this study. Therefore, the mineral assemblages of the Type-II Cpx and feldspar crystallized in a shallow reservoir (Fig. 12).

Amp is a critical mineral phase in hydrous magmas and is stable across wide P-T conditions of 0.1–22 kbar and 700–1100 °C, respectively (Nandedkar et al., 2014; Ridolfi and Renzulli, 2011; Krawczynski et al., 2011). Type-I Amp core and rim are also in disequilibrium with the corresponding whole rocks in this study, as they have lower Mg# values compared to those of the whole rocks (Fig. 11b). The amphibole-melt thermobarometer is thus not suitable for crystallization P-T calculations (Putirka, 2016). The crystallization temperatures of Type-I Amp were calculated using the pressure-independent thermometer (equation 5 of Putirka, 2016), and yield temperatures of 996–1076 °C in the core and 971–1013 °C in the rim. The single-Amp thermometer proposed by Ridolfi et al. (2021) was also used for comparison and show indistinguishable results. The single-amphibole barometer of Ridolfi et al. (2021) is appropriate for Amp with high MgO (generally Mg# > 50), thus the core of Type-I

Amp in this study are constrained to have crystallized at pressures of 4.0–5.0 kbar (Fig. 12). Those Type-I Amp rims show low Mg# and Eu/Eu* values corresponding to the shallow level crystallization with plagioclase saturation.

To investigate whether the lamprophyres were formed through a single magma differentiation in a closed system or magma mixing in an open system, we utilized GeoPS (Fig. 12a) (Xiang and Connolly, 2022) to model the process of magma evolution. The results of the modeling show that neither in a hydrous nor in an anhydrous magma system, and a single liquid line of descent cannot interpret the mineral compositions and P-T conditions of lamprophyres. Instead, the mineral assemblages in the lamprophyres likely formed by multiple magma replenishment (Fig. 12a). The Type-I Cpx grains were cumulates that crystallized in an anhydrous mafic magma reservoir, while the Amp crystallized in a hydrous mafic magma reservoir. These distinct magma reservoirs were also supported by the trace elements of Cpx and Amp, i.e., Amp grains exhibit significantly Nb and Ta positive anomalies, but Type-I Cpx show no Nb and Ta anomalies. On the other hand, the Type-II Cpx and feldspar crystallized in an alkaline magma reservoir. This is further supported by the fact that Type-I Amp rim has higher K_2O contents than Type-I Amp core (Fig. 10). Furthermore, the Kfs core show higher orthoclase contents than the Kfs rim also demonstrating the magmas with high alkaline contents recharged into the shallow magma reservoir.

The P-T conditions recorded by coexisting minerals and modeling results reveal multiple stages of magma storage for the lamprophyres. These estimated crystallization temperatures and pressures are consistent with the crystallization sequence of magmatic mineral phases that inferred by mineral textual features and geochemical data. These diverse-origin minerals were assembled during transport and emplacement, suggesting that they did not form through closed systems. Rather, they represent a crystal mush that underwent open system processes, such as multiple magma replenishment episodes or percolating melts.

Reconstruction of the transcrustal magmatic system for the lamprophyres

According to the disequilibrium mineral-melt textures and the pressure-temperature calculations for mineral crystallization, we propose a petrogenetic model of a transcrustal magmatic system with multiple magma reservoirs at different crustal depths to interpret the formation of the lamprophyres. As illustrated in Fig. 13, an anhydrous mafic magma, derived from the mantle, ascended through regional faults and stalled at the lower crust with a depth of 30–40 km, leading to the formation of a crystal mush through the crystallization of Mg-rich Type-I Cpx in the first-level magma reservoir. Subsequently, a hydrous mafic magma ascended through peripheral conduits, passing through the crystal-dominated mush zone of the first-level magma reservoir and potentially stalling at a depth of ~15 km. The ascending magmas carried early-formed Type-I Cpx crystals to the second-level magma reservoir in the middle crust, where they were consumed in a peritectic reaction, resulting in the formation of a high Mg# Amp core. Plagioclase was not produced in this magma reservoir due to the high pressures and water contents. Meanwhile, apatite became saturated at this magma reservoir and formed as Ap inclusions within the Amp core. Subsequently, the second-level magma reservoir was subject to an alkaline magma replenishment from a deeper magma storage region, transporting the Cpx-bearing Amp and Ap to a shallower magma reservoir at a depth of < 10 km. As the slightly evolved melts ascended to shallower levels in the upper crust, they reached water saturation, promoting the crystallization of plagioclase and K-feldspar under low pressure and temperature conditions. In the shallower third-level magma reservoir, the evolved magmas produced a low Mg# Amp rim and Fe-rich Type-II Cpx. The presence of acicular Ap and groundmass texture in the studied samples probably recorded a fast magma ascent rate in the upper crust level (Costa et al., 2013; Li et al., 2020). Therefore, the magma plumbing system of lamprophyres in this study includes at least three levels of magma reservoirs extending throughout the crust (Fig. 13). The ascending recharged magmas captured antecrysts and phenocrysts from multiple magma reservoirs at various crustal levels, resulting in the aggregation of minerals with contrasting crystallization histories within the host melts.

IMPLICATIONS

The whole-rock compositions of the lamprophyre dykes are significantly influenced by the proportion and type of antecrysts in the samples. It is important to note that high MgO contents in the whole-rock samples may not necessarily indicate the composition of the parental magmas, as they can result from low MgO magmas with a high proportion of MgO-rich antecrysts (Ubide et al., 2014b). In addition, the whole-rock geochemical data of lamprophyre dykes show absence of Eu/Eu* anomalies in this study (Fig. 5), implying that plagioclase differentiation did not occur during magma evolution. However, the trace elements of both Type-I Amp rim and Type-II Cpx have low Eu/Eu* and Sr/Sr* values, strongly indicating the occurrence of plagioclase differentiation in the magma system, which was concealed by whole-rock trace elements. Furthermore, the two types of Cpx have variable degrees of negative Nb and Ta anomalies, whereas the whole-rock compositions of lamprophyre show OIB-like trace element patterns with positive Nb and Ta anomalies, which could be inherited from the compositions of Amp phenocrysts.

Amp commonly appears as a hydrous mineral phase during the differentiation of arc magmas and has been identified in arc root complexes (Bouilhol et al., 2015; Dessimoz et al., 2012) and cumulates captured by arc lavas (Cooper et al., 2016; Klaver et al., 2017; Smith, 2014; Wang et al., 2019). It can be formed by a peritectic reaction that consumes precursor Cpx. Previous studies suggest that arc magma differentiation is significantly controlled by "cryptic amphibole fractionation", as amphibole breakdown rapidly when magma rises near the surface, outside the amphibole stability field (Davidson et al., 2007a; Rutherford and Hill, 1993). Thus, amphibole is a rare phenocryst phase in volcanic arc rocks, although it may be abundant in the deep crust cumulates. Amphibole fractionation in the deep magma reservoirs significantly modifies the geochemical features of arc magmas. Our study manifests that the fractionation of reaction-replacement Amp can also occur within the alkaline magmas system in the intraplate setting, which has not been demonstrated in previous studies. The presence of amphibole within mid-upper crustal magma reservoirs suggests that mid-upper crystal mushes can act as a sponge for water dissolved from mantle-derived magmas (Davidson et al., 2007a).

ACKNOWLEDGEMENTS

The present study was financially supported by the National Natural Science Foundation of Hebei province (No. D2020402013), Science and Technology Project of Hebei Education Department (BJ2020023), National Natural Science Foundation of China (41872082, 41730213, 41890831, and 42372080), Hong Kong Research Grant Council (17302317 and 17307918), HKU Internal Grants for Member of Chinese Academy of Sciences (102009906) and for Distinguished Research Achievement Award (102010100), the fundamental research funds for the Central Universities (2652018116 and 2652018135), a project from Guangdong Province (2019QN01H101), and the CAS "Light of West China" Program (2018-XBYJRC-003). We thank Kehong Cai and Kai Wang for their kind helps during fieldwork. This work is a contribution of the Joint Laboratory of Chemical Geodynamics between the University of Hong Kong and Guangzhou Institute of Geochemistry, Chinese Academy of Sciences.

Appendix A. Supplementary data

Supplementary data to this article can be found online at

REFERENCES CITED

Aigner-Torres, M., Blundy, J., Ulmer, P., and Pettke, T., 2007, Laser Ablation ICPMS study of trace element partitioning between plagioclase and basaltic melts: an experimental approach: Contributions to Mineralogy and Petrology, v. 153, no. 6, p. 647-667, 10.1007/s00410-006-0168-2.

Anderson, K.R., Johanson, I.A., Patrick, M.R., Gu, M., Segall, P., Poland, M.P., Montgomery-Brown, E.K., Miklius, A., 2019. Magma reservoir failure and the onset of caldera collapse at Kilauea Volcano in 2018. Science 366. 10.1126/science.aaz1822.

Arculus, R. J., and Wills, K. J., 1980, The petrology of plutonic blocks and inclusions from the Lesser Antilles island arc: Journal of Petrology, v. 21, no. 4, p. 743-799.

Bachmann, O., Huber, C., 2016. Silicic magma reservoirs in the Earth's crust. American Mineralogist 101, 2377-2404. 10.2138/am-2016-5675.

Blatter, D. L., Sisson, T. W., and Hankins, W. B., 2013, Crystallization of oxidized, moderately hydrous arc basalt at mid- to lower-crustal pressures: implications for andesite genesis: Contributions to Mineralogy and Petrology, v. 166, no. 3, p. 861-886, 10.1007/s00410-013-0920-3.

Blatter, D. L., Sisson, T. W., and Hankins, W. B., 2017, Voluminous arc dacites as amphibole reaction-boundary liquids: Contributions to Mineralogy and Petrology, v. 172, no. 5, 10.1007/s00410-017-1340-6.

Bottazzi, P., Tiepolo, M., Vannucci, R., Zanetti, A., Brumm, R., Foley, S., and Oberti, R., 1999, Distinct site preferences for heavy and light REE in amphibole and the prediction of Amph/LDREE: Contributions to Mineralogy & Petrology, v. 137, no. 1, p. 36-45.

Bouilhol, P., Schmidt, M. W., and Burg, J. P., 2015, Magma Transfer and Evolution in Channels within the Arc Crust: the Pyroxenitic Feeder Pipes of Sapat (Kohistan, Pakistan): Journal of Petrology, v. 56, no. 7, p. 1309-1342, 10.1093/petrology/egv037.

Bryan, S.E., Peate, I.U., Peate, D.W., Self, S., Jerram, D.A., Mawby, M.R., Marsh, J.S., Miller, J.A., 2010. The largest volcanic eruptions on Earth. Earth-Science Reviews 102, 207-229. 10.1016/j.earscirev.2010.07.001.

Cashman, K., and Blundy, J., 2013, Petrological cannibalism: the chemical and textural consequences of incremental magma body growth: Contributions to Mineralogy and Petrology, v. 166, no. 3, p. 703-729, 10.1007/s00410-013-0895-0.

Cashman, K.V., Giordano, G., 2014. Calderas and magma reservoirs. Journal of Volcanology and Geothermal Research 288, 28-45. 10.1016/j.jvolgeores.2014.09.007.

Cashman, K. V., Sparks, R. S., and Blundy, J. D., 2017, Vertically extensive and unstable magmatic systems: A unified view of igneous processes: Science, v. 355, no. 6331, 10.1126/science.aag3055.

Christensen, N. I., and Mooney, W. D., 1995, Seismic velocity structure and composition of the continental crust: A global view: Journal of Geophysical

Research: Solid Earth, v. 100, no. B6, p. 9761-9788.

Cooper, G. F., Davidson, J. P., and Blundy, J. D., 2016, Plutonic xenoliths from Martinique, Lesser Antilles: evidence for open system processes and reactive melt flow in island arc crust: Contrib Mineral Petrol, v. 171, no. 10, p. 87, 10.1007/s00410-016-1299-8.

Cooper, K. M., and Kent, A. J., 2014, Rapid remobilization of magmatic crystals kept in cold storage: Nature, v. 506, no. 7489, p. 480-483, 10.1038/nature12991.

Costa, F., Andreastuti, S., Bouvet de Maisonneuve, C., and Pallister, J. S., 2013, Petrological insights into the storage conditions, and magmatic processes that yielded the centennial 2010 Merapi explosive eruption: Journal of Volcanology and Geothermal Research, v. 261, p. 209-235, 10.1016/j.jvolgeores.2012.12.025.

Costa, F., Coogan, L. A., and Chakraborty, S., 2009, The time scales of magma mixing and mingling involving primitive melts and melt–mush interaction at mid-ocean ridges: Contributions to Mineralogy and Petrology, v. 159, no. 3, p. 371-387, 10.1007/s00410-009-0432-3.

Dai, H. K., Oliveira, B., Zheng, J. P., Griffin, W. L., Afonso, J. C., Xiong, Q., and O'Reilly, S. Y., 2021, Melting Dynamics of Late Cretaceous Lamprophyres in Central Asia Suggest a Mechanism to Explain Many Continental Intraplate Basaltic Suite Magmatic Provinces: Journal of Geophysical Research: Solid Earth, v. 126, no. 4, 10.1029/2021jb021663.

Daly, R. A., The nature of volcanic action, *in* Proceedings Proceedings of the

American Academy of Arts and Sciences1911, Volume 47, JSTOR, p. 47-122.

Davidson, J., Turner, S., Handley, H., MacPherson, C., and Dosseto, A., 2007a, Amphibole “sponge” in arc crust?: Geology, v. 35, no. 9, p. 787, https://doi.org/10.1130/G23637A.1.

Davidson, J. P., Morgan, D. J., Charlier, B. L. A., Harlou, R., and Hora, J. M., 2007b, Microsampling and Isotopic Analysis of Igneous Rocks: Implications for the Study of Magmatic Systems: Annual Review of Earth and Planetary Sciences, v. 35, no. 1, p. 273-311, 10.1146/annurev.earth.35.031306.140211.

Dessimoz, M., Müntener, O., and Ulmer, P., 2012, A case for hornblende dominated fractionation of arc magmas: the Chelan Complex (Washington Cascades): Contributions to Mineralogy and Petrology, v. 163, no. 4, p. 567-589, 10.1007/s00410-011-0685-5.

Edmonds, M., Cashman, K. V., Holness, M., and Jackson, M., 2019, Architecture and dynamics of magma reservoirs: Philos Trans A Math Phys Eng Sci, v. 377, no. 2139, p. 20180298, 10.1098/rsta.2018.0298.

Gao, J., Li, M. S., Xiao, X. C., Tang, Y. Q., and He, G. Q., 1998, Paleozoic tectonic evolution of the Tianshan Orogen, northwestern China: Tectonophysics, v. 287, no. 1–4, p. 213-231, http://dx.doi.org/10.1016/S0040-1951(98)80070-X.

Grove, T. L., Elkins-Tanton, L. T., Parman, S. W., and et al., 2003, Fractional crystallization and mantle-melting controls on calc-alkaline differentiation trends: Contributions to Mineralogy and Petrology, v. 145, no. 5, p. 515-533, https://doi.org/10.1007/s00410-003-0448-z.

Han, B.-f., Liu, J.-b., and Zhang, L., 2008, A Noncognate Relationship between Megacrysts and Host Basalts from the Tuoyun Basin, Chinese Tian Shan: The Journal of Geology, v. 116, no. 5, p. 499-509, https://doi.org/10.1086/590136.

Han, Y., Zhao, G., Sun, M., Eizenhöfer, P. R., Hou, W., Zhang, X., Liu, D., Wang, B., and Zhang, G., 2015, Paleozoic accretionary orogenesis in the Paleo-Asian Ocean: Insights from detrital zircons from Silurian to Carboniferous strata at the northwestern margin of the Tarim Craton: Tectonics, v. 34, no. 2, p. 334-351, 10.1002/2014tc003668.

Han, Y. G., and Zhao, G. C., 2018, Final amalgamation of the Tianshan and Junggar orogenic collage in the southwestern Central Asian Orogenic Belt: Constraints on the closure of the Paleo-Asian Ocean: Earth-Science Reviews, v. 186, p. 129-152, https://doi.org/10.1016/j.earscirev.2017.09.012.

Icenhower, J., and London, D., 1996, Experimental partitioning of Rb, Cs, Sr, and Ba between alkali feldspar and peraluminous melt: American Mineralogist, v. 81, no. 5-6, p. 719-734, doi:10.2138/am-1996-5-619.

Ji, J. Q., Han, B. F., Fei, Z. M., Yin, C. Z., and Lin, L. Y., 2006, Cretaceous-Paleogene alkaline magmatism in Tuyon basin, southwest Tianshan mountains: geochronology, petrology and geochemistry: Acta Petrologica Sinica, v. 22, no. 5, p. 1324-1340.

Ji, W.-Q., Wu, F.-Y., Wang, J.-M., Liu, X.-C., Liu, Z.-C., Zhang, Z., Cao, W., Wang, J.-G., Zhang, C., 2020. Early Evolution of Himalayan Orogenic Belt and Generation of Middle Eocene Magmatism: Constraint From Haweng

Granodiorite Porphyry in the Tethyan Himalaya. Frontiers in Earth Science 8. 10.3389/feart.2020.00236.

Jin Li., Suo-han Tang., Xiang-kun Zhu., Chen-xu Pan. (2017). Production and Certification of the Reference MaterialGSB 04-3258-2015 as a 143Nd/144Nd Isotope Ratio Reference. Geostand. Geoanal. Res., 2017, 41, 255-262.

Jorgenson, C., Higgins, O., Petrelli, M., Begue, F., Caricchi, L., 2022. A Machine Learning-Based Approach to Clinopyroxene Thermobarometry: Model Optimization and Distribution for Use in Earth Sciences. J Geophys Res Solid Earth 127, e2021JB022904. 10.1029/2021JB022904.

Klaver, M., Matveev, S., Berndt, J., Lissenberg, C. J., and Vroon, P. Z., 2017, A mineral and cumulate perspective to magma differentiation at Nisyros volcano, Aegean arc: Contributions to Mineralogy and Petrology, v. 172, no. 11-12, 10.1007/s00410-017-1414-5.

Krawczynski, M.J., Grove, T.L., Behrens, H., 2012. Amphibole stability in primitive arc magmas: effects of temperature, H2O content, and oxygen fugacity. Contributions to Mineralogy and Petrology 164, 317-339. 10.1007/s00410-012-0740-x.

Kröner, A., Alexeiev, D. V., Rojas-Agramonte, Y., Hegner, E., Wong, J., Xia, X., Belousova, E., Mikolaichuk, A. V., Seltmann, R., Liu, D., and Kiselev, V. V., 2013, Mesoproterozoic (Grenville-age) terranes in the Kyrgyz North Tianshan: Zircon ages and Nd–Hf isotopic constraints on the origin and evolution of basement blocks in the southern Central Asian Orogen: Gondwana Research, v.

23, no. 1, p. 272-295, 10.1016/j.gr.2012.05.004.

Ladenburger, S., Marks, M. A. W., Upton, B., Hill, P., Wenzel, T., and Markl, G., 2016, Compositional variation of apatite from rift-related alkaline igneous rocks of the Gardar Province, South Greenland: American Mineralogist, v. 101, no. 3, p. 612-626, 10.2138/am-2016-5443.

Le Bas MJ, Le Maitre RW, Strekeisen A, and B, Z., 1986, A chemical classification of volcanic rocks based on the total alkali-silica diagram: Journal of petrology, v. 27, no. 3, p. 745-750.

Leake, B. E., Woolley, A. R., Arps, C. E., Birch, W. D., Gilbert, M. C., Grice, J. D., Hawthorne, F. C., Kato, A., Kisch, H. J., and Krivovichev, V. G., 1997, Nomenclature of amphiboles; report of the Subcommittee on Amphiboles of the International Mineralogical Association Commission on new minerals and mineral names: Mineralogical magazine, v. 61, no. 405, p. 295-310.

Li, C. F., Li, X. H., Li, Q. L., Guo, J. H., Yang, Y. H. (2012). Rapid and precise determination of sr and nd isotopic ratios in geological samples from the same filament loading by thermal ionization mass spectrometry employing a single-step separation scheme. Analytica Chimica Acta, 727 (10), 54–60.

Li, W., Chakraborty, S., Nagashima, K., and Costa, F., 2020, Multicomponent diffusion of F, Cl and OH in apatite with application to magma ascent rates: Earth and Planetary Science Letters, v. 550, 10.1016/j.epsl.2020.116545.

Li, X.-C., Zhou, M.-F., 2018. The nature and origin of hydrothermal REE mineralization in the Sin Quyen deposit, northwestern Vietnam. Economic

Geology 113, 645-673.

Liang, T., Luo, Z., Ke, S., Li, L., Li, W., and Zhan, H., 2004, The basaltic volcanic rocks in the Tuyon Basin, NW China: Petrogenesis and tectonic implications: Himalayan Journal of Sciences, v. 2, no. 4, p. 194-194.

Liang, T., Luo, Z. H., Ke, S., Wei, Y., Li, D. D., Huang, J. X., and Huang, F., 2007, SHRIMP zircon dating of the Tuoyon volcanoes group, Xinjiang, and its geodynamic implications: Acta Petrologica Sinica, v. 23, no. 6, p. 1381-1391.

Liu, Y., Hu, Z., Zong, K., Gao, C., Gao, S., Xu, J., Chen, H., 2010. Reappraisement and refinement of zircon U-Pb isotope and trace element analyses by LA-ICP-MS. Chinese Science Bulletin 55, 1535-1546. https://doi.org/10.1007/s11434-010-3052-4.

Lin J., Liu Y.S., Yang Y.H., Hu Z.C. (2016). Calibration and correction of LA-ICP-MS and LA-MC-ICP-MS analyses for element contents and isotopic ratios. Solid Earth Sciences, 1, 5–27.

Loiselet, C., Husson, L., Braun, J., 2009. From longitudinal slab curvature to slab rheology. Geology 37, 747-750. https://doi.org/10.1130/g30052a.1.

Melekhova, E., Blundy, J., Robertson, R., and Humphreys, M. C. S., 2015, Experimental Evidence for Polybaric Differentiation of Primitive Arc Basalt beneath St. Vincent, Lesser Antilles: Journal of Petrology, v. 56, no. 1, p. 161-192, 10.1093/petrology/egu074.

Morimoto, N., Fabries, J., Ferguson, A., Ginzburg, I., Ross, M., Seifert, F., Zussman, J., Aoki, K., and Gottardi, G., 1988, Nomenclature of pyroxenes:

Mineralogical magazine, v. 52, no. 367, p. 535-550.

Müntener, O., and Ulmer, P., 2006, Experimentally derived high-pressure cumulates from hydrous arc magmas and consequences for the seismic velocity structure of lower arc crust: Geophysical Research Letters, v. 33, no. 21, 10.1029/2006gl027629.

Nandedkar, R. H., Ulmer, P., and Müntener, O., 2014, Fractional crystallization of primitive, hydrous arc magmas: an experimental study at 0.7 GPa: Contributions to Mineralogy and Petrology, v. 167, no. 6, 10.1007/s00410-014-1015-5.

Neave, D. A., Bali, E., Guðfinnsson, G. H., Halldórsson, S. A., Kahl, M., Schmidt, A.-S., and Holtz, F., 2019, Clinopyroxene–Liquid Equilibria and Geothermobarometry in Natural and Experimental Tholeiites: the 2014–2015 Holuhraun Eruption, Iceland: Journal of Petrology, v. 60, no. 8, p. 1653-1680, 10.1093/petrology/egz042.

Neave, D. A., and Putirka, K. D., 2017, A new clinopyroxene-liquid barometer, and implications for magma storage pressures under Icelandic rift zones: American Mineralogist, v. 102, no. 4, p. 777-794, 10.2138/am-2017-5968.

Owen, J. P., 2007, Geochemistry of lamprophyres from the Western Alps, Italy: implications for the origin of an enriched isotopic component in the Italian mantle: Contributions to Mineralogy and Petrology, v. 155, no. 3, p. 341-362, 10.1007/s00410-007-0246-0.

Paton, C., Woodhead, J.D., Hellstrom, J.C., Hergt, J.M., Greig, A., Maas, R., 2010.

Improved laser ablation U-Pb zircon geochronology through robust downhole fractionation correction. Geochemistry, Geophysics, Geosystems 11, n/a-n/a. 10.1029/2009gc002618.

Pichavant, M., and Macdonald, R., 2007, Crystallization of primitive basaltic magmas at crustal pressures and genesis of the calc-alkaline igneous suite: experimental evidence from St Vincent, Lesser Antilles arc: Contributions to Mineralogy and Petrology, v. 154, no. 5, p. 535-558, 10.1007/s00410-007-0208-6.

Putirka, K., 2016, Amphibole thermometers and barometers for igneous systems and some implications for eruption mechanisms of felsic magmas at arc volcanoes: American Mineralogist, v. 101, no. 4, p. 841-858, 10.2138/am-2016-5506.

Putirka, K. D., 2008, Thermometers and Barometers for Volcanic Systems: Reviews in Mineralogy and Geochemistry, v. 69, no. 1, p. 61-120, 10.2138/rmg.2008.69.3.

Reubi, O., and Blundy, J., 2009, A dearth of intermediate melts at subduction zone volcanoes and the petrogenesis of arc andesites: Nature, v. 461, no. 7268, p. 1269-1273, 10.1038/nature08510.

Rhodes, J., Dungan, M., Blanchard, D., and Long, P. J. T., 1979, Magma mixing at mid-ocean ridges: evidence from basalts drilled near 22 N on the Mid-Atlantic Ridge, v. 55, no. 1-2, p. 35-61.

Ridolfi, F., 2021, Amp-TB2: An Updated Model for Calcic Amphibole Thermobarometry: Minerals, v. 11, no. 3, 10.3390/min11030324.

Ridolfi, F., and Renzulli, A., 2011, Calcic amphiboles in calc-alkaline and alkaline magmas: thermobarometric and chemometric empirical equations valid up to 1,130°C and 2.2 GPa: Contributions to Mineralogy and Petrology, v. 163, no. 5, p. 877-895, 10.1007/s00410-011-0704-6.

Ridolfi, F., Zanetti, A., Renzulli, A., Perugini, D., Holtz, F., and Oberti, R., 2018, AMFORM, a new mass-based model for the calculation of the unit formula of amphiboles from electron microprobe analyses: American Mineralogist, v. 103, no. 7, p. 1112-1125, 10.2138/am-2018-6385.

Rock, N. M., 1987, The nature and origin of lamprophyres: an overview: Geological Society, London, Special Publications, v. 30, no. 1, p. 191-226.

Rutherford, M. J., and Hill, P. M. J. J. o. G. R. S. E., 1993, Magma ascent rates from amphibole breakdown: an experimental study applied to the 1980–1986 Mount St. Helens eruptions, v. 98, no. B11, p. 19667-19685.

Russell, W.A., Papanastassiou, D.A., Tombrello, T.A., (1978). Ca isotope fractionation on the earth and other solar system materials. Geochim. Cosmochim. Acta, 42 (8), 1075–1090.

Simonov, V. A., Mikolaichuk, A. V., Rasskazov, S. V., and Kovyazin, S. V., 2008, Cretaceous-Paleogene within-plate magmatism in Central Asia: data from the Tien Shan basalts: Russian Geology and Geophysics, v. 49, no. 7, p. 520-533, 10.1016/j.rgg.2008.06.009.

Simonov, V. A., Mikolaichuk, A. V., Safonova, I. Y., Kotlyarov, A. V., and Kovyazin, S. V., 2015, Late Paleozoic–Cenozoic intra-plate continental basaltic magmatism of the Tienshan–Junggar region in the SW Central Asian Orogenic Belt: Gondwana Research, v. 27, no. 4, p. 1646-1666, 10.1016/j.gr.2014.03.001.

Sisson, T., and Grove, T., 1993, Experimental investigations of the role of H2O in calc-alkaline differentiation and subduction zone magmatism: Contributions to mineralogy petrology, v. 113, no. 2, p. 143-166.

Sisson, T. W., Ratajeski, K., Hankins, W. B., and Glazner, A. F., 2005, Voluminous granitic magmas from common basaltic sources: Contributions to Mineralogy and Petrology, v. 148, no. 6, p. 635-661, 10.1007/s00410-004-0632-9.

Smith, D. J., 2014, Clinopyroxene precursors to amphibole sponge in arc crust: Nat Commun, v. 5, p. 4329, 10.1038/ncomms5329.

Smith, J. V., and Brown, W. L., 1989, Feldspar Minerals: 1. Crystal Structures, Physical, Chemical, and Microtextural Properties. 2nd Edition. Berlin, Heidelberg and New York (Springer-Verlag), 1988. xviii + 828 pp., 352: Mineralogical Magazine, v. 53, no. 373, p. 655-656, 10.1180/minmag.1989.053.373.21.

Sobel, E. R., and Arnaud, N., 2000, Cretaceous–Paleogene basaltic rocks of the Tuyon basin, NW China and the Kyrgyz Tian Shan: the trace of a small plume: Lithos, v. 50, no. 1-3, p. 191-215.

Sparks, R. S. J., Annen, C., Blundy, J. D., Cashman, K. V., Rust, A. C., and Jackson, M. D., 2019, Formation and dynamics of magma reservoirs: Philos Trans A Math Phys Eng Sci, v. 377, no. 2139, p. 20180019, 10.1098/rsta.2018.0019.

Sun, S. S., and McDonough, W. F., 1989, Chemical and Isotopic Systematics of Oceanic Basalts: Implications for Mantle Composition and Processes: Geological Society London Special Publications, v. 42, no. 1, p. 313-345, https://doi.org/10.1144/GSL.SP.1989.042.01.19.

Tiepolo, M., Oberti, R., Zanetti, A., Vannucci, R., and Foley, S. F., 2007, Trace-Element Partitioning Between Amphibole and Silicate Melt: Reviews in Mineralogy and Geochemistry, v. 67, no. 1, p. 417-452, 10.2138/rmg.2007.67.11.

Ubide, T., Arranz, E., Lago, M., Galé, C., and Larrea, P., 2012, The influence of crystal settling on the compositional zoning of a thin lamprophyre sill: A multi-method approach: Lithos, v. 132-133, p. 37-49, 10.1016/j.lithos.2011.11.012.

Ubide, T., Galé, C., Arranz, E., Lago, M., and Larrea, P., 2014a, Clinopyroxene and amphibole crystal populations in a lamprophyre sill from the Catalonian Coastal Ranges (NE Spain): A record of magma history and a window to mineral-melt partitioning: Lithos, v. 184-187, p. 225-242, 10.1016/j.lithos.2013.10.029.

Ubide, T., Galé, C., Larrea, P., Arranz, E., and Lago, M., 2014b, Antecrysts and their effect on rock compositions: The Cretaceous lamprophyre suite in the Catalonian Coastal Ranges (NE Spain): Lithos, v. 206-207, p. 214-233, 10.1016/j.lithos.2014.07.029.

Ubide, T., Mollo, S., Zhao, J. X., Nazzari, M., Scarlato, P., 2019. Sector-zoned clinopyroxene as a recorder of magma history, eruption triggers, and ascent rates. Geochimica et Cosmochimica Acta 251, 265-283. 10.1016/j.gca.2019.02.021.

Ulmer, P., Kaegi, R., and Müntener, O., 2018, Experimentally Derived Intermediate to Silica-rich Arc Magmas by Fractional and Equilibrium Crystallization at 1·0 GPa: an Evaluation of Phase Relationships, Compositions, Liquid Lines of Descent and Oxygen Fugacity: Journal of Petrology, v. 59, no. 1, p. 11-58, 10.1093/petrology/egy017.

Wang, J., Wang, Q., Dan, W., Yang, J.-H., Yang, Z.-Y., Sun, P., Qi, Y., and Hu, W.-L., 2019, The role of clinopyroxene in amphibole fractionation of arc magmas: Evidence from mafic intrusive rocks within the Gangdese arc, southern Tibet: Lithos, v. 338-339, p. 174-188, 10.1016/j.lithos.2019.04.013.

Wang, X. S., Cai, K., Sun, M., Zhao, G. C., Xiao, W. J., and Xia, X. P., 2020, Evolution of Late Paleozoic Magmatic Arc in the Yili Block, NW China: Implications for Oroclinal Bending in the Western Central Asian Orogenic Belt: Tectonics, v. 39, no. 12, 10.1029/2019tc005822.

Wang, Y., Wang, Y., Liu, X., Fu, D., Xiao, X., and Qi, L., 2000, Geochemical characteristics and genesis of Late Cretaceous to Paleoene basalts in Tuyon basin, South Tianshan Mountain: Acta Petrrologica et Mineralogica.

White, R., and McCausland, W., 2016, Volcano-tectonic earthquakes: A new tool for estimating intrusive volumes and forecasting eruptions: Journal of Volcanology and Geothermal Research, v. 309, p. 139-155, 10.1016/j.jvolgeores.2015.10.020.

Windley, B. F., Alexeiev, D., Xiao, W. J., Kröner, A., and Badarch, G., 2007, Tectonic models for accretion of the Central Asian Orogenic Belt: Journal of the Geological Society, v. 164, p. 31-47, https://doi.org/10.1144/0016-76492006-022.

Xiao, W. J., Windley, B. F., Sun, S., Li, J. L., Huang, B. C., Han, C. M., Yuan, C., Sun, M., and Chen, H. L., 2015, A Tale of Amalgamation of Three Permo-Triassic Collage Systems in Central Asia: Oroclines, Sutures, and Terminal Accretion: Annual Review of Earth and Planetary Sciences, v. 43, no. 1, p. 477-507, https://doi.org/10.1146/annurev-earth-060614-105254.

Xing, C. M., and Wang, C. Y., 2020, Periodic mixing of magmas recorded by oscillatory zoning of the clinopyroxene macrocrysts from an ultrapotassic lamprophyre dyke: Journal of Petrology, 10.1093/petrology/egaa103.

Xu, X., Xia, L., Xia, Z., He, S., and Ma, Z., 2003, Geochemistry and genesis of Cretaceous-Paleogene basalts from the Tuoyun basin, southwest Tianshan mountains: Geochimica, v. 32, no. 6, p. 551-560.

Zhang, J., Davidson, J. P., Humphreys, M. C. S., Macpherson, C. G., and Neill, I., 2015, Magmatic Enclaves and Andesitic Lavas from Mt. Lamington, Papua New Guinea: Implications for Recycling of Earlier-fractionated Minerals through Magma Recharge: Journal of Petrology, v. 56, no. 11, p. 2223-2256, 10.1093/petrology/egv071.

Zhang W., Hu Z.C. (2020). Estimation of isotopic reference values for pure materials and geological reference materials. At. Spectrosc. 2020, 41 (3), 93–102.

Zhang W., Hu Z.C., Liu Y.S. (2020). Iso-Compass: new freeware software for isotopic data reduction of LA-MC-ICP-MS. J. Anal. At. Spectrom., 2020, 35, 1087–1096.

Figure caption

Fig. 1. (a) Simplified geological map of the western Tianshan orogenic belt and its adjacent areas (modified after 1:1000000 geological map of the Xinjiang Province and its neighboring areas in Central Asia, Xinjiang Research Center for Mineral Resources). The five-pointed star indicates the location of intraplate magmatism in the western Tianshan area; (b) Schematic geological map around Tuoyun basin modified after Huang et al. (2005) and Lithological stratigraphic section around Tuoyun basin. Q, K, J, C and S indicate Quaternary, Cretaceous, Jurassic, Carboniferous, and Silurian strata, respectively.

Fig. 2. (a and b) Field photos and (c and d) photomicrographs under cross-polarized light of lamprophyre dykes. Amp: Amphibole; Cpx: clinopyroxene; Pl: Plagioclase.

Fig. 3. (a) Tera-Wasserburg Concordia diagram, and (b) Backscattered electron image of the apatite grains in this study. Dashed red circles indicate the analytical spots for the U-Pb ages.

Fig. 4. (a) ($K_2O + Na_2O$) versus SiO_2 (Le Bas MJ et al., 1986), and (b) K_2O versus SiO_2 classification diagrams (Rock, 1987) for the lamprophyre dykes. The basalts intruded by the lamprophyres plot for comparison in (a) (Han et al., 2008; Ji et al.,

2006; Wang et al., 2000; Xu et al., 2003).

Fig. 5. Chondrite-normalized REE and primitive mantle-normalized multi-element patterns for the lamprophyre dykes (a–b), Cpx (c–d), and Amp (e–f). Normalizing values are from Sun and McDonough, (1989).

Fig. 6. Back-scattered electron images of the mineral assemblages within the lamprophyre dyke. (a–d) Type-I Cpx enclosed by Amp; (e–f) Type-II Cpx microlites; (g) The euhedral and acicular Ap grains; (h–i) Kfs with sieve texture showing a patchy-zoned core with abundant spongy spaces, which are filled with apatite; and compositional profiles of Kfs are shown in lower right side.

Fig. 7. (a) Wo–En–Fs diagram for clinopyroxene (Morimoto et al., 1988); (b) Mg#–Si diagram for the amphibole (Leake et al., 1997); (c) An–Ab–Or diagram for plagioclase from the lamprophyre dykes (Smith and Brown, 1989).

Fig. 8. Backscattered electron images (position of the microprobe analysis traverses is shown by yellow dotted line), and compositional profiles for representative Amp phenocrysts of the lamprophyre dykes.

Fig. 9. Diagrams showing the major and trace element variations within Cpx from the lamprophyre dykes. (a) TiO_2 versus Mg#; (b) Al_2O_3 versus Mg#; (c) FeO versus Mg#; (d) Eu/Eu* versus Sr/Sr* ($2Sr_{PM}/[Ce_{PM}+Nd_{PM}]$); (e) Dy/Yb versus Ti/Ti* ($2Ti_{PM}/[Sm_{PM}+Tb_{PM}]$); (f) Dy/Yb versus Dy. The trends modeled by the GeoPS reactive fractional crystallization process. We assume sample C19TY28 as starting compositions. Numbers associated with the crystallization trends correspond to crystallization temperatures. Arrows indicate Cpx trace element compositional

variations due to the fractionation of different minerals or mineral assemblages.

Fig. 10. Diagrams showing the major and trace element variations within Amp from the lamprophyre dykes. (a) TiO_2 versus Mg#; (b) Al_2O_3 versus Mg#; (c) K_2O versus Mg#; (d) ^{IV}Al versus Mg#; (e) Eu/Eu* versus Sr/Sr*; (f) Dy/Yb versus Dy. The trends modeled by the GeoPS reactive hydrous fractional crystallization process. We assume sample C19TY28 as starting compositions. Numbers associated with the crystallization trends correspond to crystallization temperatures.

Fig. 11. Equilibrium tests between minerals and their host rocks of the lamprophyre dykes in the Tuoyun basin. (a) Mg# in clinopyroxene versus Mg# in whole-rock; (b) Mg# in amphibole versus Mg# in whole-rock. The dotted curves (Rhodes et al., 1979) represent the range of equilibrium compositions between mineral and melt using an Fe-Mg distribution coefficient of 0.28 ± 0.08 for clinopyroxene (Putirka, 2008) and 0.28 ± 0.11 for amphibole (Putirka, 2016).

Fig. 12. (a) Mg# versus Pressure diagram. The trends modeled by the GeoPS showing hydrous and anhydrous fractional crystallization processes. We assume sample C19TY28 as starting compositions. Numbers associated with the crystallization trends correspond to crystallization temperatures. (b) Pressure-Temperature estimates of clinopyroxene and amphibole crystallization for the lamprophyre dykes in the Tuoyun basin. The clinopyroxene-only thermobarometer proposed by Jorgenson et al. (2022) can be used to estimate the crystallization temperature and pressure of the Type-I Cpx and Type-II Cpx. The crystallization temperatures and pressures of Amp core were calculated using pressure-independent thermometer equation (5) of Putirka (2016)

DOI: https://doi.org/10.2138/am-2023-9271. http://www.minsocam.org/

(equivalent to the results from single-amp thermometer of Ridolfi et al. (2021)), and single-amp barometer from Ridolfi et al. (2021), respectively. The depth corresponding to pressure is labelled on the right. Note that crust density is assumed to be 2.8 g/cm^3 (Christensen and Mooney, 1995).

Fig. 13. Schematic diagrams showing a possible transcrustal magmatic system for the lamprophyre dykes in the Tuoyun basin.

Figure 1

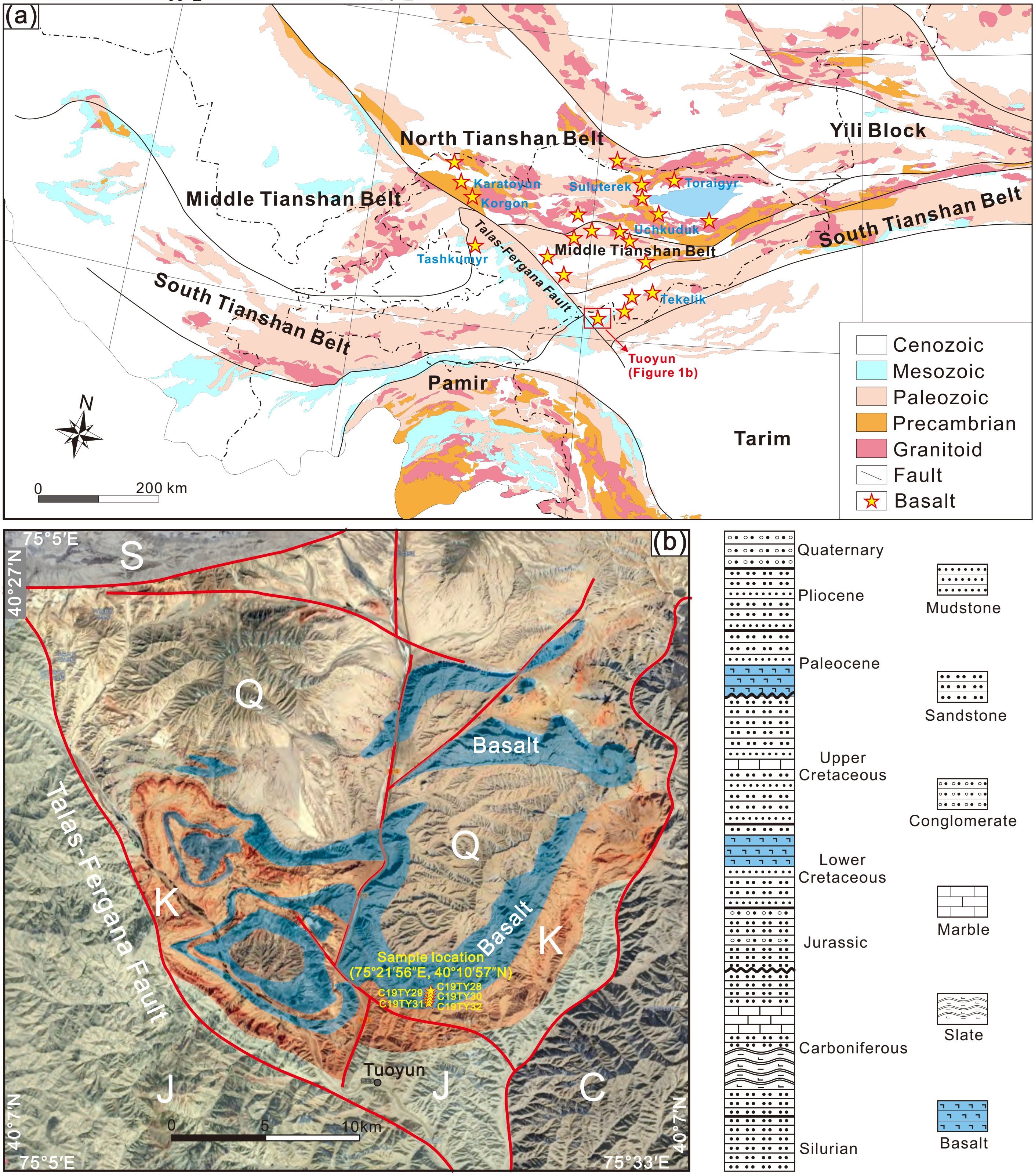
(a)
65°E
70°E
75°E
80°E
44°N
40°N
North Tianshan Belt
Middle Tianshan Belt
South Tianshan Belt
Yili Block
South Tianshan Belt
Middle Tianshan Belt
Talas-Fergana Fault
Karatoyun
Korgon
Tashkumyr
Suluterek
Toraigyr
Uchkuduk
Tekelik
Tuoyun
(Figure 1b)
Pamir
Tarim
N
0
200 km
Cenozoic
Mesozoic
Paleozoic
Precambrian
Granitoid
Fault
Basalt
(b)
75°5′E
40°27′N
S
Q
Basalt
Q
Talas-Fergana Fault
K
Basalt
K
Sample location
(75°21′56″E, 40°10′57″N)
C19TY29
C19TY31
C19TY28
C19TY30
C19TY32
Tuoyun
J
J
C
0
5
10km
40°7′N
75°5′E
75°33′E
40°7′N
Quaternary
Pliocene
Paleocene
Upper
Cretaceous
Lower
Cretaceous
Jurassic
Carboniferous
Silurian
Mudstone
Sandstone
Conglomerate
Marble
Slate
Basalt

Figure 2

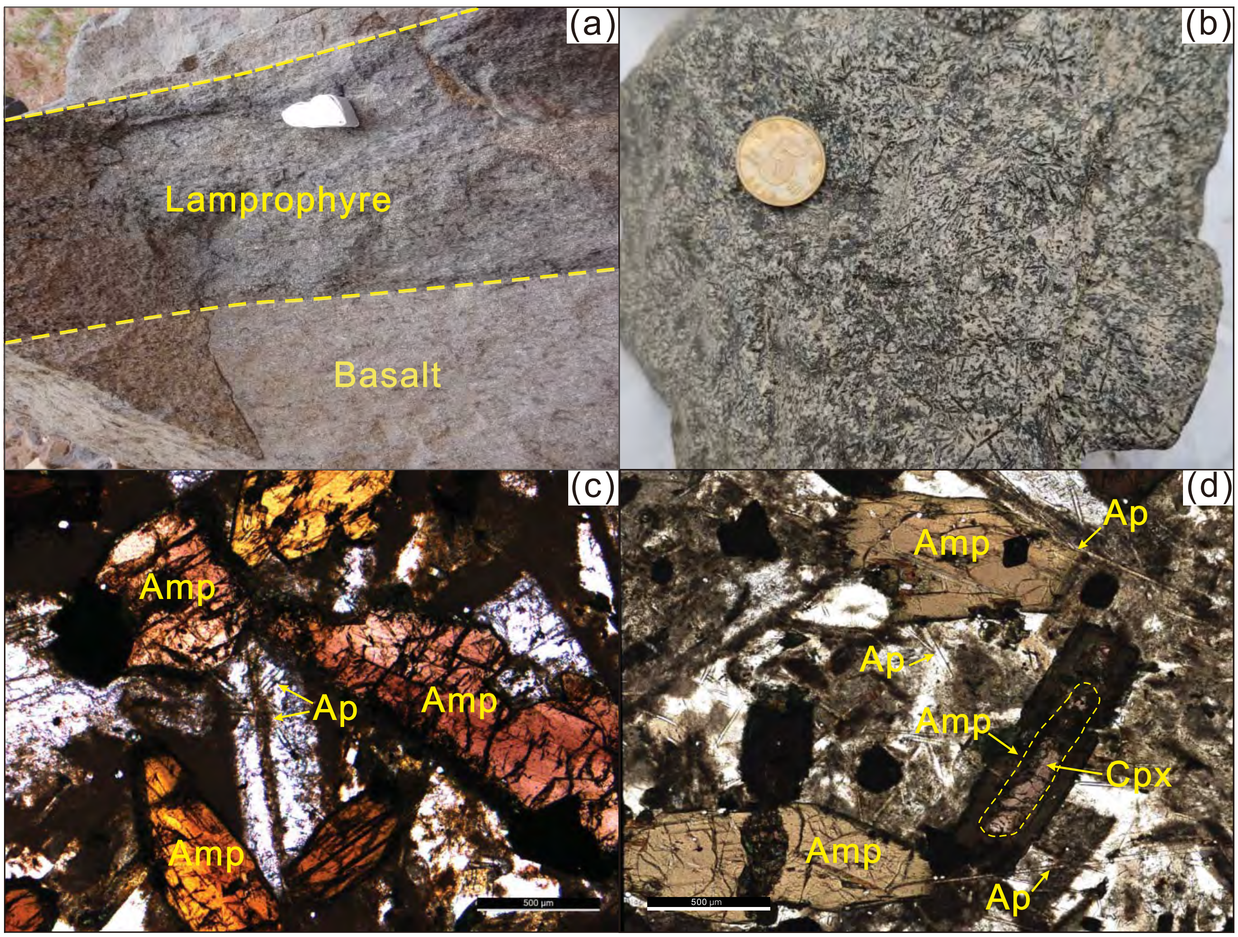
(a)
Lamprophyre
Basalt
(b)
(c)
Amp
Ap
Amp
Amp
500 µm
(d)
Ap
Amp
Ap
Amp
Cpx
Amp
Ap
500 µm

Figure 3

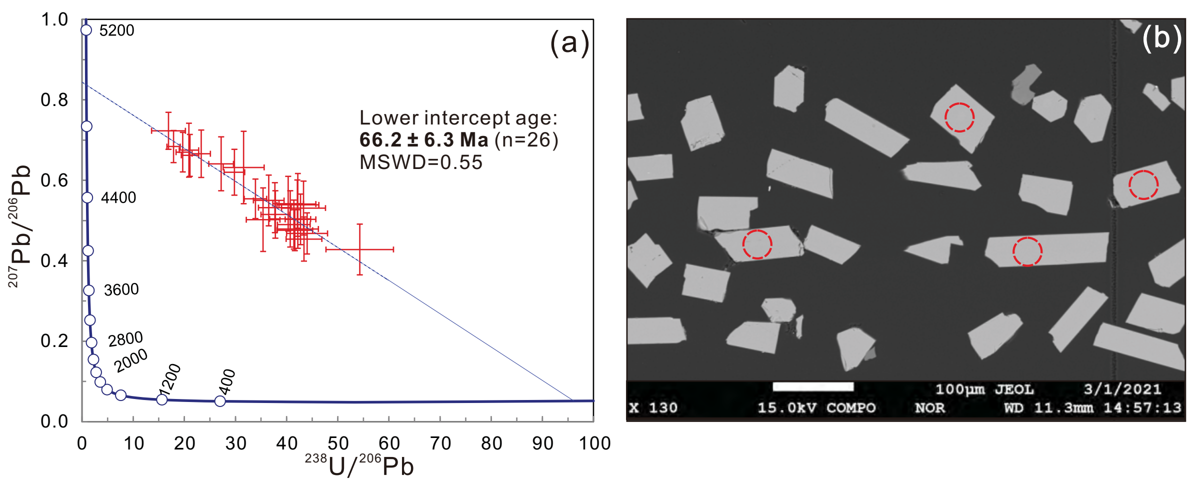
(a)
Lower intercept age:
66.2 ± 6.3 Ma (n=26)
MSWD=0.55
5200
4400
3600
2800
2000
1200
400
$^{207}Pb/^{206}Pb$
$^{238}U/^{206}Pb$
1.0
0.8
0.6
0.4
0.2
0.0
0
10
20
30
40
50
60
70
80
90
100
(b)
100μm JEOL 3/1/2021
X 130 15.0kV COMPO NOR WD 11.3mm 14:57:13

Figure 4

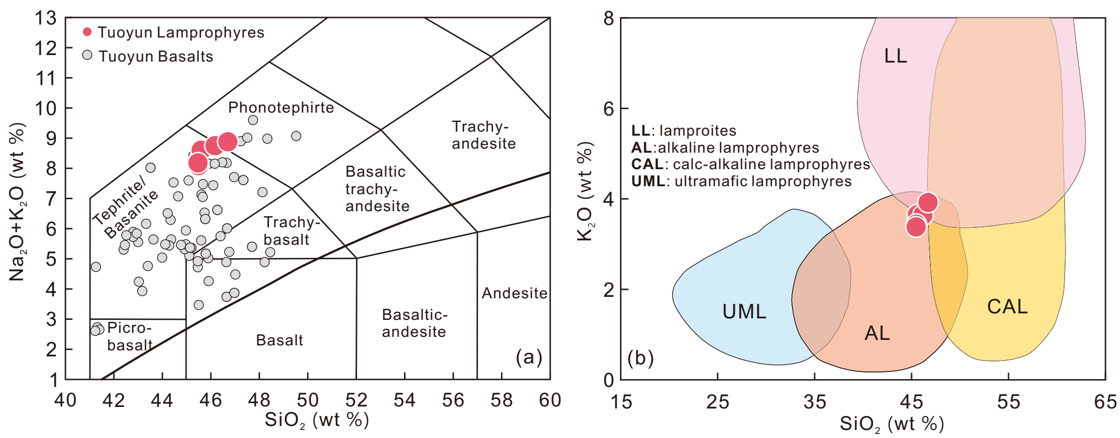
Tuoyun Lamprophyres
Tuoyun Basalts
Phonotephirte
Trachy-andesite
Basaltic trachy-andesite
Tephrite/Basanite
Trachy-basalt
Picro-basalt
Basalt
Basaltic-andesite
Andesite
(a)
Na2O+K2O (wt %)
SiO2 (wt %)
LL
LL: lamproites
AL:alkaline lamprophyres
CAL: calc-alkaline lamprophyres
UML: ultramafic lamprophyres
UML
AL
CAL
(b)
K2O (wt %)
SiO2 (wt %)

This is the peer-reviewed, final accepted version for American Mineralogist, published by the Mineralogical Society of America.
The published version is subject to change. Cite as Authors (Year) Title. American Mineralogist, in press.
DOI: https://doi.org/10.2138/am-2023-9271. http://www.minsocam.org/

Figure 5

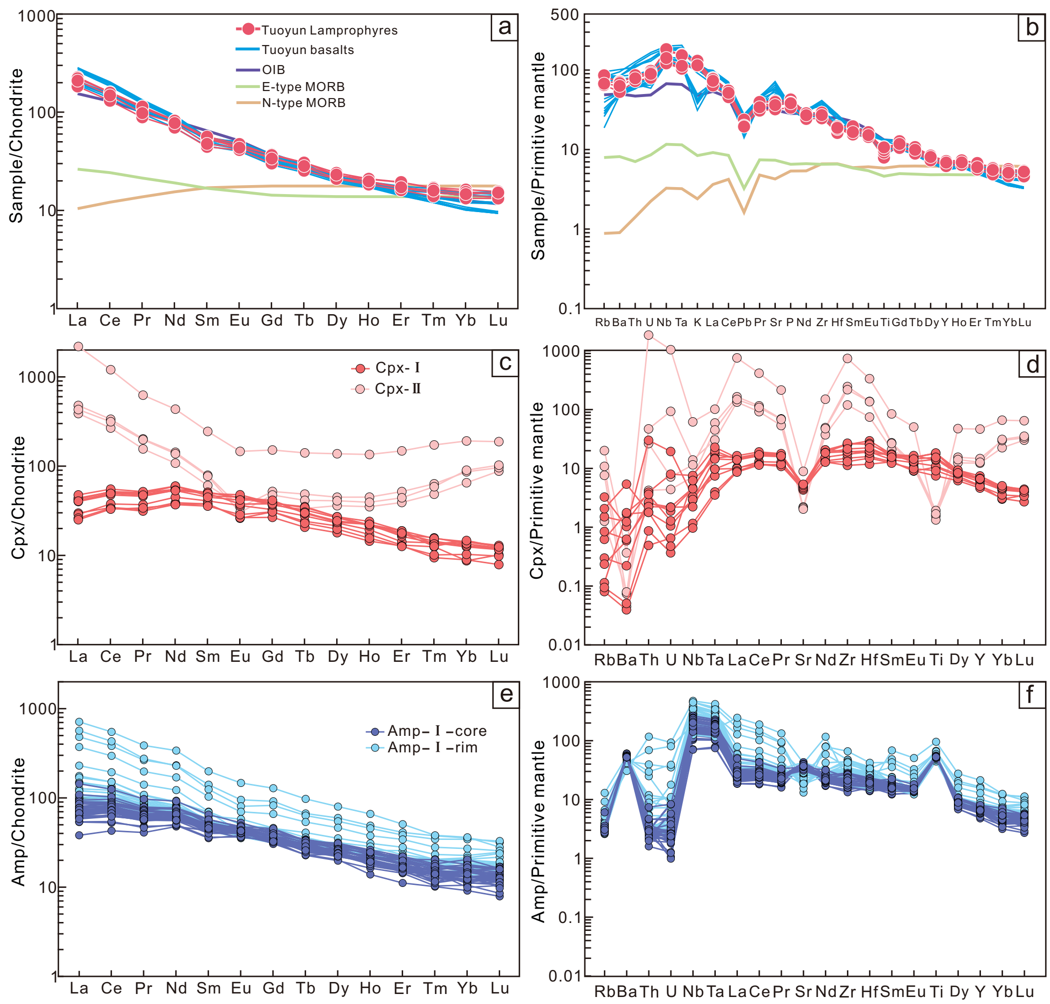

This is the peer-reviewed, final accepted version for American Mineralogist, published by the Mineralogical Society of America.
The published version is subject to change. Cite as Authors (Year) Title. American Mineralogist, in press.
DOI: https://doi.org/10.2138/am-2023-9271. http://www.minsocam.org/

Figure 6

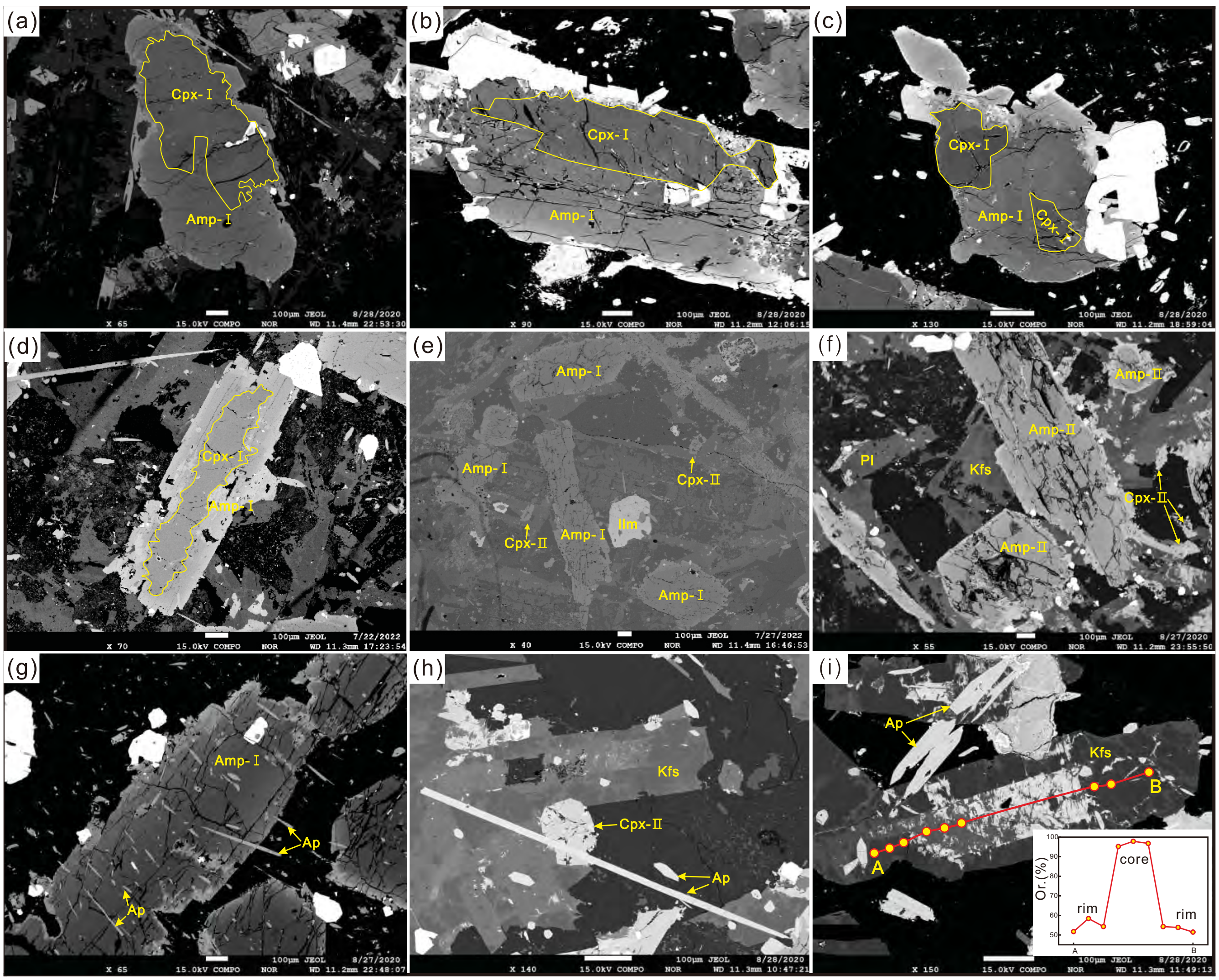

Figure 7

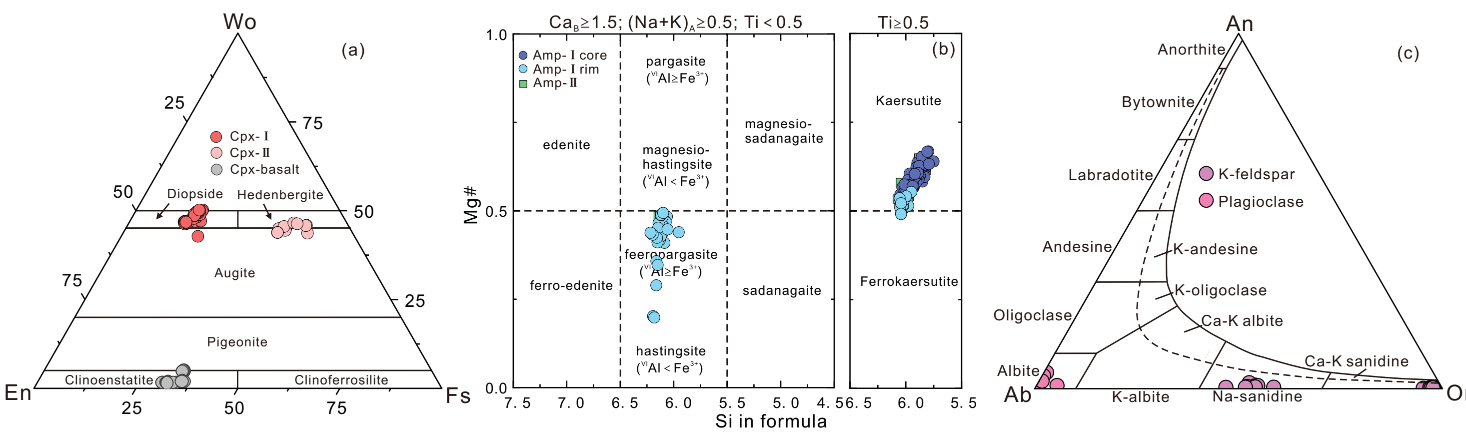
Wo
(a)
Cpx- I
Cpx- II
Cpx-basalt
Diopside
Hedenbergite
Augite
Pigeonite
Clinoenstatite
Clinoferrosilite
En
Fs
Ca$_B$≥1.5; (Na+K)$_A$≥0.5; Ti<0.5
Ti≥0.5
(b)
Amp- I core
Amp- I rim
Amp- II
pargasite
edenite
magnesio-hastingsite
magnesio-sadanagaite
feeropargasite
ferro-edenite
sadanagaite
hastingsite
Kaersutite
Ferrokaersutite
Mg#
Si in formula
An
(c)
Anorthite
Bytownite
Labradotite
Andesine
Oligoclase
Albite
K-feldspar
Plagioclase
K-andesine
K-oligoclase
Ca-K albite
Ca-K sanidine
K-albite
Na-sanidine
Ab
Or

Figure 8

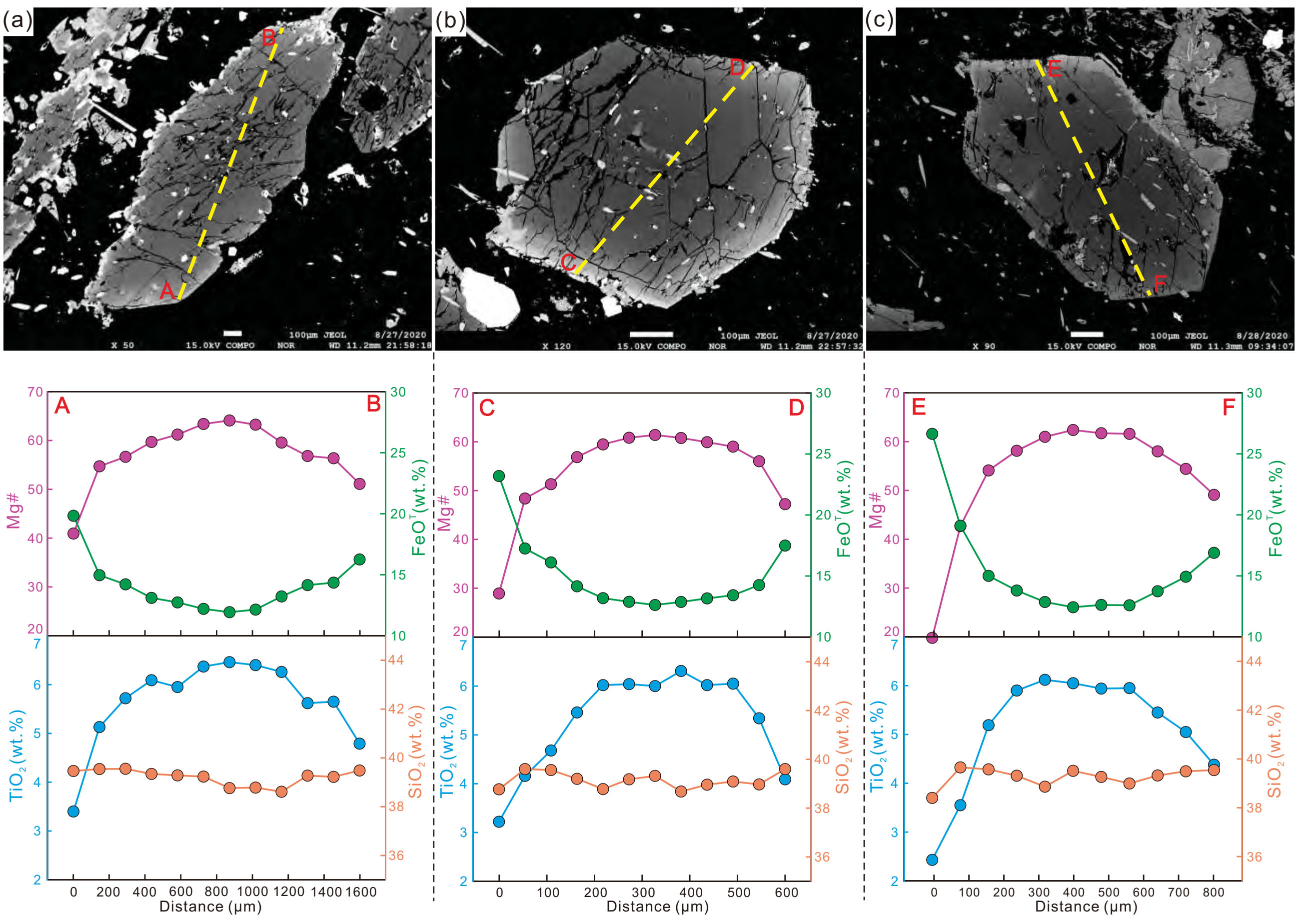

Figure 9

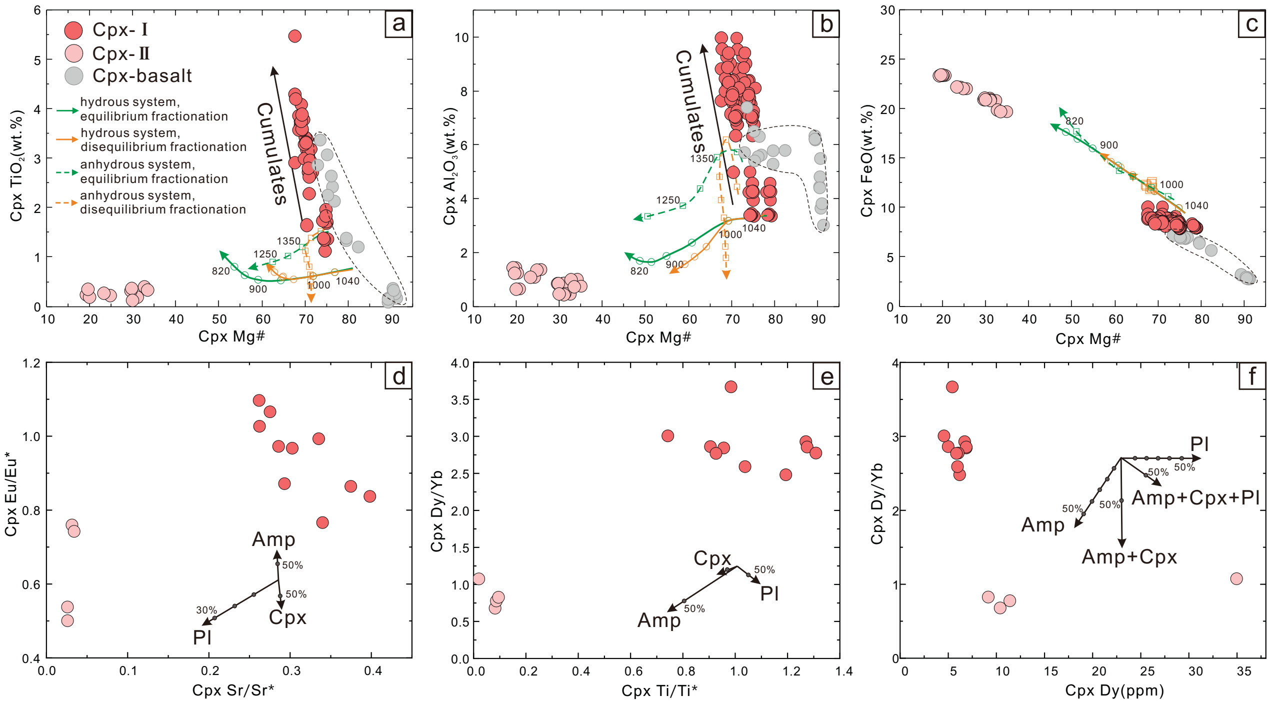
Cpx- I
Cpx- II
Cpx-basalt
hydrous system, equilibrium fractionation
hydrous system, disequilibrium fractionation
anhydrous system, equilibrium fractionation
anhydrous system, disequilibrium fractionation
Cumulates
Cpx TiO2(wt.%)
Cpx Al2O3(wt.%)
Cpx FeO(wt.%)
Cpx Mg#
Cpx Eu/Eu*
Cpx Sr/Sr*
Cpx Dy/Yb
Cpx Ti/Ti*
Cpx Dy(ppm)
Amp
Cpx
Pl
Amp+Cpx+Pl
Amp+Cpx
a
b
c
d
e
f

Figure 10

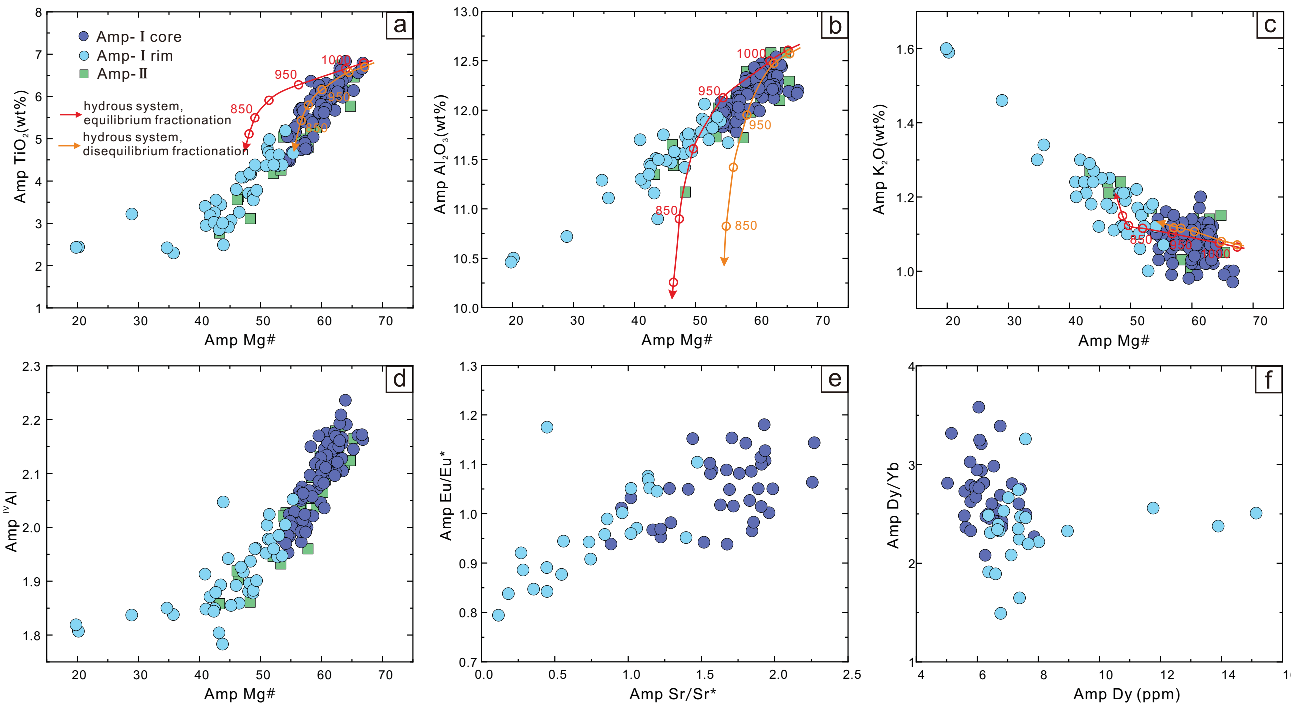
a
Amp- I core
Amp- I rim
Amp- II
hydrous system, equilibrium fractionation
hydrous system, disequilibrium fractionation
Amp TiO2(wt%)
Amp Mg#
b
Amp Al2O3(wt%)
Amp Mg#
c
Amp K2O(wt%)
Amp Mg#
d
Amp IVAl
Amp Mg#
e
Amp Eu/Eu*
Amp Sr/Sr*
f
Amp Dy/Yb
Amp Dy (ppm)

Figure 11

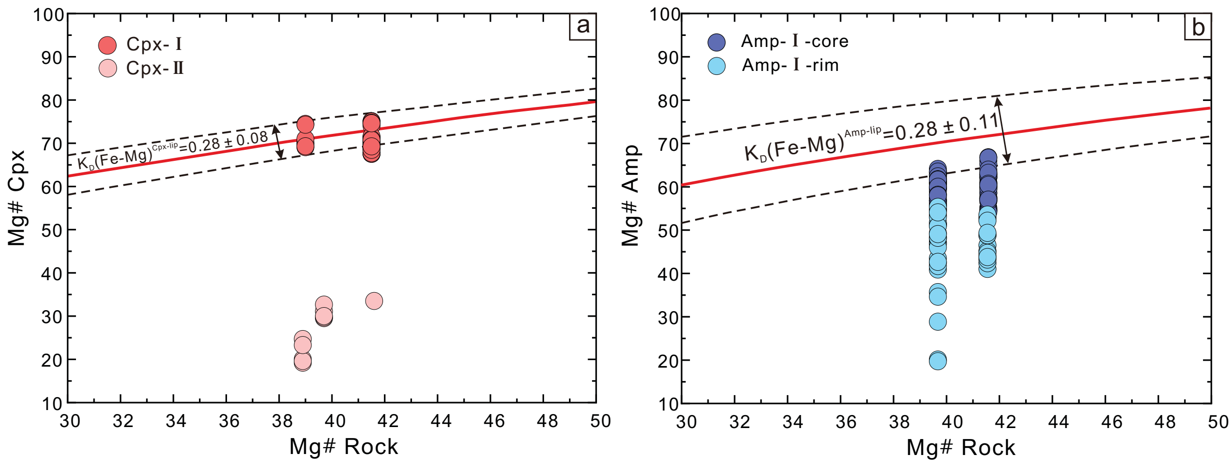
a
Cpx- I
Cpx- II
K_D(Fe-Mg)^Cpx-lip=0.28 ± 0.08
Mg# Cpx
Mg# Rock
b
Amp- I -core
Amp- I -rim
K_D(Fe-Mg)^Amp-lip=0.28 ± 0.11
Mg# Amp
Mg# Rock

Figure 12

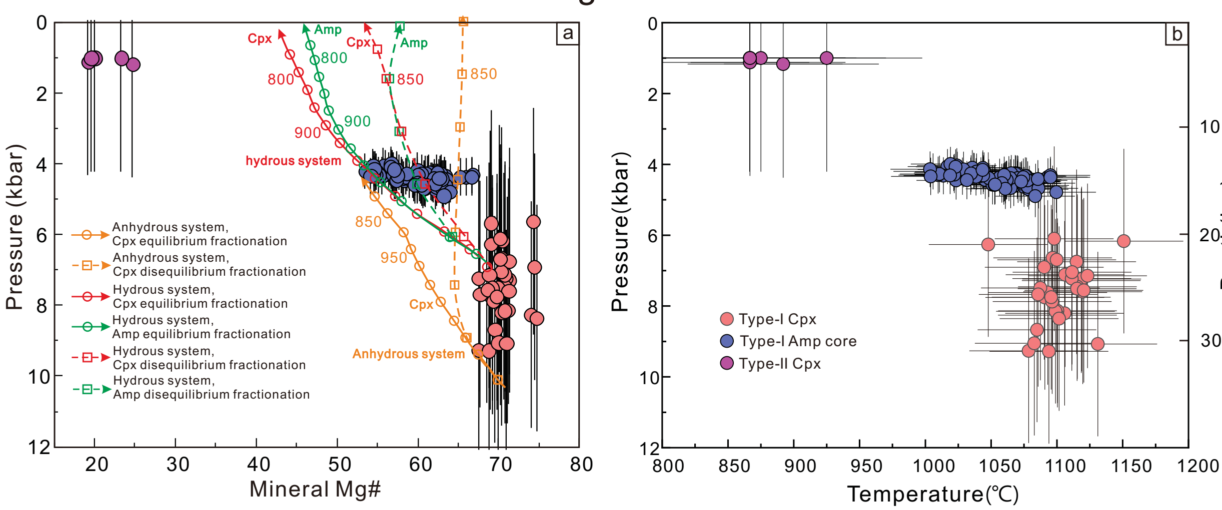
a
Pressure (kbar)
Mineral Mg#
Cpx
Amp
800
850
900
950
hydrous system
Anhydrous system
Anhydrous system, Cpx equilibrium fractionation
Anhydrous system, Cpx disequilibrium fractionation
Hydrous system, Cpx equilibrium fractionation
Hydrous system, Amp equilibrium fractionation
Hydrous system, Cpx disequilibrium fractionation
Hydrous system, Amp disequilibrium fractionation
b
Pressure(kbar)
Depth(km)
Temperature(℃)
Type-I Cpx
Type-I Amp core
Type-II Cpx

Figure 13

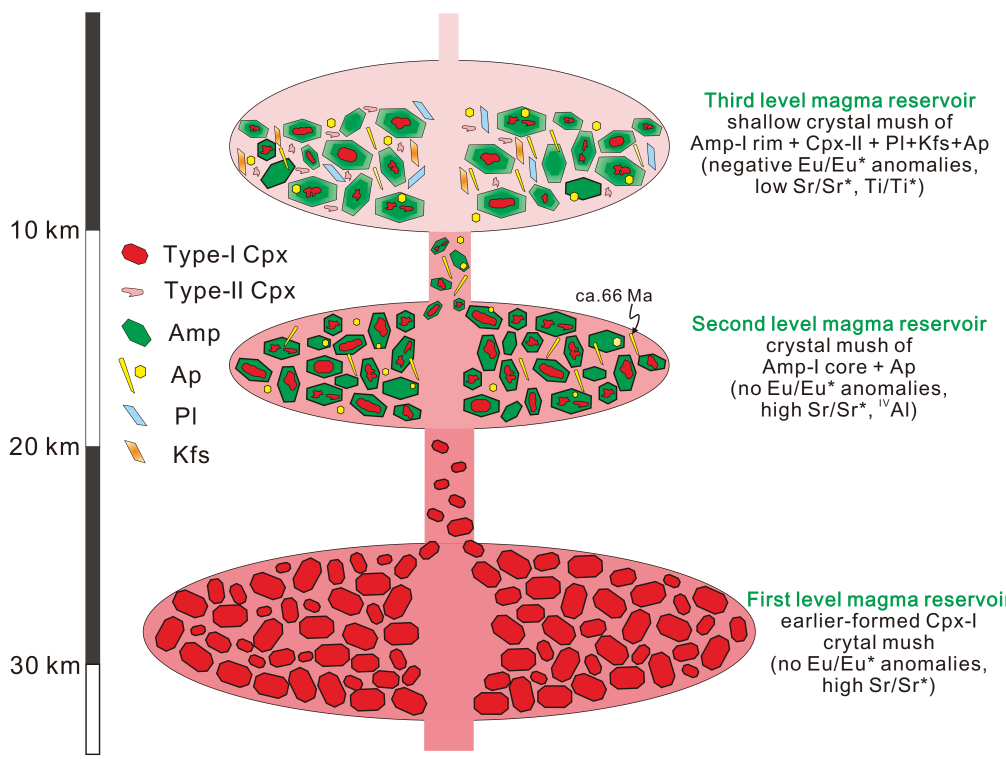
Third level magma reservoir
shallow crystal mush of
Amp-I rim + Cpx-II + Pl+Kfs+Ap
(negative Eu/Eu* anomalies,
low Sr/Sr*, Ti/Ti*)
10 km
Type-I Cpx
Type-II Cpx
Amp
Ap
Pl
Kfs
ca.66 Ma
Second level magma reservoir
crystal mush of
Amp-I core + Ap
(no Eu/Eu* anomalies,
high Sr/Sr*, IVAl)
20 km
First level magma reservoir
earlier-formed Cpx-I
crytal mush
(no Eu/Eu* anomalies,
high Sr/Sr*)
30 km